ULTRA-LOW-COST BROAD-BAND NEAR-INFRARED SILICON PHOTODETECTORS BASED ON HOT ELECTRONS

A THESIS SUBMITTED TO

THE GRADUATE SCHOOL OF ENGINEERING AND SCIENCE

OF BILKENT UNIVERSITY

IN PARTIAL FULFILLMENT OF THE REQUIREMENTS FOR

THE DEGREE OF

MASTER OF SCIENCE

IN

ELECTRICAL AND ELECTRONICS ENGINEERING

By

Mohammad Amin Nazirzadeh

January, 2015

ULTRA-LOW-COST BROAD-BAND NEAR-INFRARED SILICON
PHOTODETECTORS BASED ON HOT ELECTRONS

By Mohammad Amin Nazirzadeh

January, 2015

We certify that we have read this thesis and that in our opinion it is fully adequate,
in scope and in quality, as a thesis for the degree of Master of Science.

_____

Assist. Prof. Dr. Ali Kemal Okyay (Advisor)

_____

Assoc. Prof. Dr. Vakur B. Ertürk

_____

Assoc. Prof. Dr. Ceyhun Bulutay

Approved for the Graduate School of Engineering and Science:

_____

Prof. Dr. Levent Onural
Director of the Graduate School

ABSTRACT

ULTRA-LOW-COST BROAD-BAND NEAR-INFRARED SILICON PHOTODETECTORS BASED ON HOT ELECTRONS

Mohammad Amin Nazirzadeh

M.S. in Electrical and Electronics Engineering

Advisor: Assist. Prof. Dr. Ali Kemal Okyay

January, 2015

Silicon is at the heart of all of the end-user digital devices such as smart phones, laptops, and wearable technologies. It is the holy grail for the large-scale production of semiconductor devices since start of the semiconductor era due to its relatively good electrical, mechanical and chemical properties. Silicon's mediocre optical properties also make it an acceptable material for energy harvesting and ultraviolet photodetection applications. But its relatively large bandgap ($1.12\ eV$) makes it infrared blind. So Silicon photodetectors fail to detect infrared light using traditional techniques. Hence, an all-Silicon solution is of interest for low-cost civil applications like telecommunication and imaging. Silicon based Schottky junction is a promising candidate for infrared photodetection. Internal photoemission is the main mechanism of photodetection in the Schottky junctions. Incident photons elevate the kinetic energy of the electrons in the metal so that the energetic electrons can jump over the Schottky barrier or tunnel through it. Carefully designed metal contact of the Schottky junction can, at the same time, give rise to hot electron generation through plasmon resonances. Here we introduce ultra-low-cost broad-band near-infrared Silicon photodetectors with a study over types of metal and nanostructures and fabrication techniques. The devices exhibit photoresponsivity as high as $2\ mA/W$ and $600\ \mu A/W$ at $1300\ nm$ and $1550\ nm$ wavelengths, and can see beyond $2000\ nm$ wavelengths. Their dark current density is as low as $50\ pA/\mu m^2$. Simplicity and scalability of fabrication in this type of structures make them the most cost effective infrared detectors due to lack of expensive fabrication steps such as sub-micron lithography and high temperature epitaxial growth techniques.

Keywords: Photodetector, Plasmonic, Near Infrared, Silicon, Broad-band.

ÖZET

SICAK ELEKTRON TEMELLİ DÜŞÜK MALİYETLİ GENİŞ BANT YAKIN KIZILÖTESİ SİLİSYUM FOTODEDEKTÖRLER

Mohammad Amin Nazirzadeh

Elektrik ve Elektronik Mühendisliği, Yüksek Lisans

Tez Danışmanı: Assist. Prof. Dr. Ali Kemal Okyay

Ocak, 2015

Silisyum; nihai kullanıcı ürünü olan akıllı telefonlar, dizüstü bilgisayarlar ve giyilebilen teknolojiler gibi tüm dijital cihazların kalbinde yer almaktadır. Yarıiletken çağının başlangıcından beri, nispeten iyi elektiriksel, mekanik ve kimyasal özelliklerinden dolayı büyük ölçekli yarıiletken cihazların üretiminde temel madde olarak bilinmektedir. Silisyumun vasat optik özellikleri ise enerji eldesinde ve morötesi fotodedektör uygulamalarında kabul görmesini sağlamaktadır. Fakat nispeten büyük enerji bandı aralığı (1.12 eV) sebebiyle, geleneksel yöntemler kullanarak kızılötesi dalgaboylarında çalışan Silisyum foto-dedektörler üretmek mümkün olmamıştır. Bundan dolayı, telekomünikasyon ve görüntüleme gibi düşük maliyet gerektiren kamu uygulamalarında kullanılmak üzere tamamı Silisyum teknolojisi ile üretilebilen fotodedektörler elde etmek büyük önem kazanmıştır. Kızılötesi bölgesinde foto algılama için, Silisyum tabanlı Schottky eklem aygıtlar umut verici bir aday olarak görülmektedir. Schottky eklem aygıtlarda foto algılama, iç fotoemisyon ile gerçekleşir. Gelen fotonlar metal içerisindeki elektronların kinetik enerjisini yükselterek, elektronların Schottky bariyerini atlamasına veya tünelleme yoluyla geçmesine sebep olur. Ayrıca Schottky eklemin metal kontak kısmının şekli uygun biçimde tasarlanarak plazmon rezonansları tetiklenebilir ve sıcak elektron üretimi önemli ölçüde artırılabilir. Biz bu çalışmada oldukça düşük maliyetli, geniş bantta, yakın kızılötesi bölgesinde Schottky eklem Silisyum fotodedektörleri, bu yapılar üzerindeki plazmonik etkileri, metal ve nanoyapıların çeşitlerini ve fabrikasyon teknikleri inceleyeceğiz. Bu cihazlar, 1300 nm ve 1500 nm dalgaboylarında sırasıyla 2 mA/W ve 600 $\mu A/W$ fototepki göstermekte ve 2000 nm dalga boyunun ötesine kadar ışığa tepki verebilmektedir. Karanlık akım yoğunluğu da 50 $pA/\mu m^2$ kadar düşüktür. Mikron-altı litografi ve yüksek sıcaklıkta epitaksiyel

büyütme teknikleri gibi oldukça pahalı fabrikasyon aşamaları kullanılmamakta, fabrikasyon kolaylığı ve ölçeklenebilir üretim sayesinde maliyet etkin kızılötesi dedektörler elde edilmektedir.

Anahtar sözcükler: Fotodedektör, Plazmonik, Yakın kızılötesi, Silisyum, Geniş-Bant.

Acknowledgement

I would like to express my sincere gratitude to my advisor Dr. Ali Kemal Okyay who believed in my potential as a young scientist and provided me this big opportunity to study in Bilkent University under his supervision. It was an honor to be a member of the Okyay group. I would like to thank Dr. Vakur B. Ertürk and Dr. Ceyhun Bulutay for being in my thesis committee and contributing to my thesis with their suggestions and insight.

I am grateful to my family who encouraged me throughout my life. My mother and father taught me every word about life and made it meaningful. My brother, Mohammad Javad, and my sister, Saeideh always stood by my side and supported me. Having such a family was always an honor for me. I would like to express my deepest gratitude to my beloved wife, Nasrin for all the love she gave me and for all the lovely distractions from my student life.

I would like to thank Fatih Bilge Atar and Berk Berkan Turgut for being my best friends in Turkey, who always helped me with their support and suggestions. I would like to thank all of my friends in Bilkent University for being such good friends for me, specially Maryam Salim for her friendliness and kindness. Many thanks to Okyay group members and my office colleagues, specially Şeyma Canik, Levent Erdal Aygün, Sami Bolat, Furkan Çimen, Yunus Emre Kesim, Muhammad Maiz Ghauri, Enes Battal, Ayşe Özcan, Seda Kizir, and Hamit Eren.

To my family and beloved wife...

Contents

List of Figures

List of Tables

Chapter 1

Introduction

1.1 Motivation

Photodetectors are one of the vital modern world elements forming a big part of our everyday life. Majority of people carry at least 5 millions of photodetectors on their phone's camera. Photodetectors are essential in taking a photo and googling a cooking instruction since long range communications are possible through intercontinental optical fibers. Near-infrared (NIR) photodetectors have great potential in end-user applications which can change the way people interact with outer world. Since these applications need both acquisition and processing available in a single unit at a low cost, today's commercial NIR photodetectors are not able to address these challenges. Usually, NIR photodetectors are made of III-V material systems [1–3], so hybrid integration with CMOS technology needs chip-to-chip bonding which further increases the cost of the system. Hence, there is a need for fabrication methods which can fulfill the demand for monolithic integration with CMOS technology as well as simplicity and scalability to decrease the final price of the NIR photodetectors. Commercial NIR photodetectors are widely used in space applications [4], night surveillance [5], telecommunication [6,7], plant health monitoring [8], food analysis [9], spectroscopy [10], and

other important applications. Provided that we have the ability to fabricate low-cost NIR photodetectors, we can make these technologies tangible for everyone.

Plant health monitoring is one of the applications of NIR imaging. NIR light is reflected from the healthy plant cells as well as the green light which enables us to understand the health of the plants using NIR cameras (Fig. 1.1) [8].
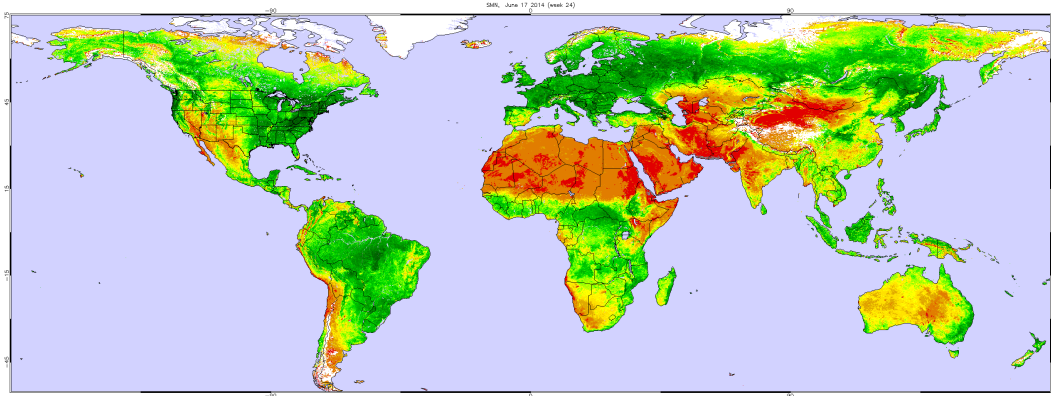
Figure 1.1: Vegetation map created by National Oceanic and Atmospheric Administration (NOAA) using satellite NIR imaging. The image shows the normalized difference vegetation index (NDVI) map of the world in June 17, 2014 [11].

Passive optical networks (PON) emerged to bring the optical fibers to the home (fiber to the home or FTTH) in order to increase the bandwidth of internet at end-user node. This approach has been developed further and has brought the fiber to a single computer (fiber to the desktop or FTTD). Gigabit passive optical network (GPON) is the next-generation of PON which is able to distribute the bandwidth dynamically through a single fiber at higher than 1 *Gbps* to multiple nodes which decreases the price of the bandwidth for people. But this systems are suffering from high cost of the optical transceivers which hinders the spread of optical fibers to every home.

Germanium-based integrated photodetectors have been studied extensively [12–18] and the first hybrid Silicon-Germanium avalanche photodetector was reported in 2008 in collaboration with Intel [19]. Short distance optical data transmission is under development using these technologies to increase the transmission bandwidth to terabit level. For example, the transmission of data between the computers in a server or even within a single computer can be done

through optical fibers. Recently Intel created the first hybrid integrated end-to-end optical transmission line to be used in future servers [20] and has increased the bandwidth of these cables to 1.6 *Tbps* in 2014 [21].

Figure 1.2: An optical connection created by Intel in 2010 [20].

Silicon is the best solution for decreasing the cost, but Silicon is a poor absorber in infrared region effectively making Silicon photodetectors infrared blind. Due to this fact, NIR photodetection on Silicon is one of the scientific races in the last decades to achieve a viable NIR photodetector technology based on Si which should be low-cost, CMOS compatible and relatively efficient.

Schottky junction is a reliable solution to this challenge due to its built-in potential barrier at the metal-semiconductor interface which makes it possible to detect sub-bandgap photons for Silicon. Photons reaching to the metal excite energetic carriers which can make it through the Schottky barrier and contribute to the photocurrent. Since this mechanism is not so efficient, enhancement methods should be used to increase the photoresponsivity. First demonstration of Schottky photodetectors on Silicon was in 1970 by Shepherd Jr et al. [22]. In order to decrease the reflection from metal contacts and consequently enhance the absorption, waveguide structures are used to achieve in-chip photodetectors [23–26]. Sobhani et al. [27] achieved narrow-band detectors using excitation of metallic grating surface plasmon polaritons (SPP). Knight et al. [28] demonstrated polarization dependent optical nanoantennas on Silicon to achieve slightly broad-band photoresponsivity over NIR region.

1.2   Thesis Organization

In this thesis study, plasmonically enhancement of Schottky photodetectors is studied to find a technique of fabricating low-cost and broad-band near-infrared photodetectors on Silicon.

In chapter 2, a brief review of the background physics is provided. Different optical absorption mechanisms are introduced in semiconductors. Then some of the known device structures are investigated. Finally, a review on the types of the plasmon resonances is provided.

In chapter 3, fabrication methods as well as the used recipes for each step of the study is introduced.

In chapter 4, characterization methods and results of the various fabricated devices are presented. Also the bases of the home-made spectral photoresponsivity measurement setup, which was developed during this study, will be explained.

In chapter 5, actual 3D FDTD simulations of the fabricated devices as well as discussions and conclusions about the investigated photodetectors and possible future works will be presented.

Chapter 2

Device Physics

Photodetectors are electronic devices which sense light and convert it to electrical current with vast applications from telecommunications [6,7] to night surveillance [5]. Light conversion in photodetectors is done in 3 major steps [29]:

- Absorption of incident photons and generation of charge carriers

- Transport of the generated charge carriers

- Collection of the charge carriers leading to photocurrent

In this chapter we will describe important mechanisms of light absorption in semiconductors and go through different types of photodetectors. Every structure uses different mechanisms for each step introduced above.

2.1 Optical Absorption

Depending on the photodetector material and structure, different types of photon absorption can occur:

2.1.1 Direct Absorption:

An electron in valence band of a direct bandgap semiconductor, absorbs a photon jumping from valence band to conductance band (interband or band to band transition) and generates an electron-hole-pair (EHP) (Fig. 2.1). This type of absorption is possible only if the incident photon energy is equal or higher than the semiconductor bandgap energy. Also due to high number of electrons in valence band and empty states in conductance band and also since band to band transition just needs a photon to be fulfilled, this type of absorption is more efficient than the other types.
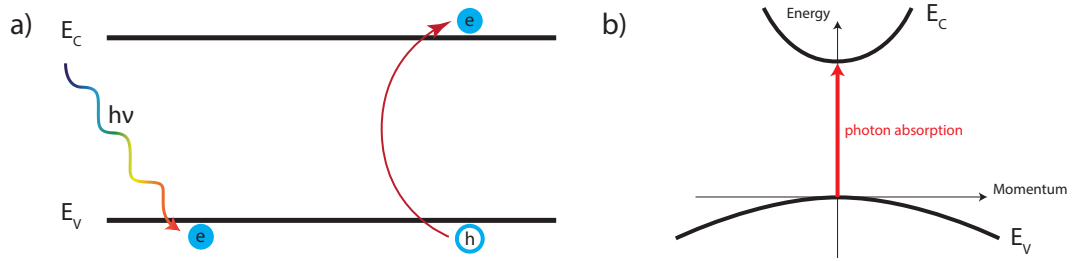
Figure 2.1: (a) Depiction of band to band transition of an electron generating an EHP (b) Band structure of a direct-bandgap semiconductor near the center of the Brillouin zone.

We can write the momentum conservation equation:

$$k_C = k_V + k_{op} \tag{2.1}$$

where k_C and k_V are the momenta of the conductance band minima and valence band maxima, respectively. From the Bloch theorem we know that the momentum of the edge of the Brillouin zone is $\frac{\pi}{a}$, where a is the unit cell dimension [30]. Also from electromagnetics we know that:

$$k_{op} = \frac{\pi}{\lambda} \tag{2.2}$$

So $k_{op} \simeq \frac{\pi}{100 \ nm} << \frac{\pi}{0.5 \ nm} \simeq \frac{\pi}{a}$ which means that the momentum of a photon is very small and that a band to band transition is a "vertical" transition in the momentum space [31]. So we can simplify the equation 2.1 to:

$$k_C \simeq k_V \tag{2.3}$$

2.1.2 Phonon Assisted Absorption:

Valence band maxima and conductance band minima do not occur at the same momentum in an indirect bandgap material. Therefore, for an interband transition to take place, an electron needs to change its momentum to be able to jump over the forbidden energy gap (Fig. 2.2). An electron can absorb a photon and make a "vertical" transition to a very short lived virtual state and then absorb a phonon and make a "horizontal" transition to the final state [32].
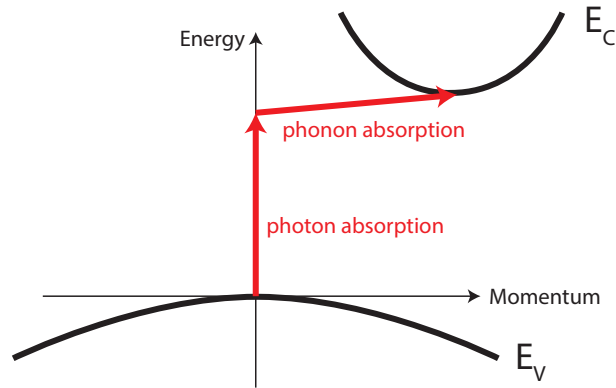
Figure 2.2: Band structure of an indirect-bandgap semiconductor near the center of the Brillouin zone. For a band to band transition, an electron should absorb both a photon and a phonon at the same time.

This absorption mechanism is not efficient because the probability of absorbing a photon and a phonon simultaneously is very low. So indirect-bandgap semiconductors are not good absorbers and as a result, they are not good emitters also.

2.1.3 Trap Assisted Absorption:

Introduction of trap centers to the mid-gap of a semiconductor increases its absorption. First a sub-bandgap photon excites an electron to the trap level. Then the excited electron gets trapped in a trap center where the electron can stay long enough time for absorbing a second photon [29]. Then the trapped electron has

the opportunity to absorb another sub-bandgap photon and get excited to the conduction band. A trap is localized in the position space which corresponds to a continuous band in the momentum space since position space and momentum space are Fourier pairs of each other [33]. So in a trap assisted absorption, two photons (not necessarily identical photons) are needed to make the transition possible making the indirect-bandgap material a more efficient absorber. Also traps let photons with lower energies to be absorbed in the semiconductor (Fig. 2.3).
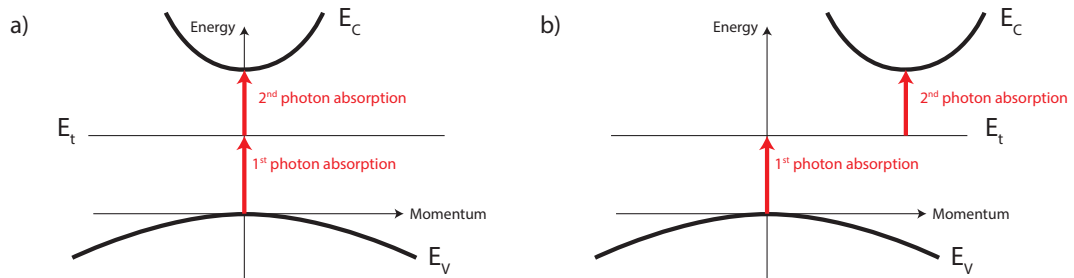
Figure 2.3: Depiction of the trap assisted absorption mechanism in (a) direct-bandgap and (b) indirect-bandgap semiconductors. The trapped electron can assume a wide range of crystal momenta, so the second transition in an indirect-bandgap semiconductor does not need phonon absorption.

2.1.4 Two Photon Absorption:

If an electron absorbs two photons simultaneously, it can jump to a virtual state and then make the second transition to the final state (Fig. 2.4). This mechanism is several orders of magnitude weaker than the direct absorption due to low probability of absorbing two photons at the same time [34].

2.1.5 Surface State Absorption:

The surface of a semiconductor is a discontinuity for the perfect crystal lattice of it. So near the surface, the energy states will be different than that of the bulk (surface states). The energy states of the surface will be further modified if we deposit another material on it (interface states). These can lie within the

8
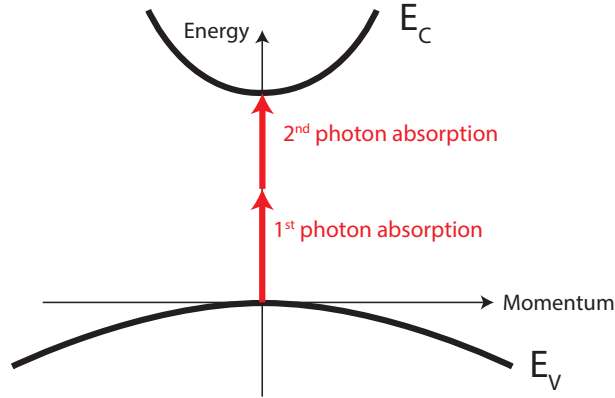
Figure 2.4: Two photon absorption illustration in the momentum space.

forbidden energy gap of the semiconductor. So they act as traps within a few atomic layers from the surface and increase the absorption near the surface of the semiconductor [35].

2.1.6 Internal Photoemission Absorption:

Photoemission is the emission of electrons from materials by shining light on them. A photon can lose its energy to an electron and give it enough energy to become a free electron. This is known as photoelectric effect first described by Einstein in 1905 [36].

Internal photoemission (IPE) is the emission of electrons from the metal to the nearby material. At the interface of a metal-semiconductor (M-S) junction, electrons with enough kinetic energy can surmount the Schottky barrier formed at the junction and get injected into the semiconductor. At 1931, Fowler published a paper describing the physics of the IPE [37]. Modifications to the Fowler theory resulted in a simpler form of the Fowler function which describes the quantum efficiency (η) of the IPE process and is in agreement with the experimental results [29, 38]:

$$\eta = C_F \frac{(h\nu - q\phi_b)^2}{h\nu} \tag{2.4}$$

where C_F is a device dependent and frequency independent coefficient called

Fowler coefficient, h is the Planck constant, q is the electron charge, ν is the incident photon frequency, and ϕ_b is the Schottky barrier height.

Photons with smaller energy than the bandgap energy of the semiconductor can excite the electrons in the conductance band to higher energy states (or the holes to deep energy levels in the valence band). Energetic carriers (hot carriers) can overcome the Schottky barrier if the normal component of their momentum to the junction is larger than a critical momentum [39].

$$P_{crit} = \sqrt{2m^*\phi_b} \tag{2.5}$$

where m^* is the effective mass of an electron in the semiconductor and ϕ_b is the Schottky barrier height.

In a Schottky junction, the Fermi level of the metal is pinned near a specific point where the interface states change from donor-like character to acceptor-like [40,41] which is known as charge neutrality level (E_{CNL}). In Silicon Schottky junctions, the Fermi level of the metal usually pin $\frac{E_g}{3}$ above the valence band [42]. So the Schottky barrier will be approximately $\frac{E_g}{3}$ for p-type Silicon and $\frac{2E_g}{3}$ for n-type Silicon which is smaller than the bandgap energy.

So IPE is the main mechanism behind the sub-bandgap absorption in photodetectors [27,28,43]. Photons with energies lower than semiconductor bandgap energy can excite hot electrons (or hot holes) which can surmount the Schottky barrier or tunnel through it, generating photocurrent (Fig. 2.5).

2.2   Photodetectors

Photodetectors are devices which absorb optical signals and generate photocurrent. Photodetection has various applications while each of them needs particular structure and figure of merit.
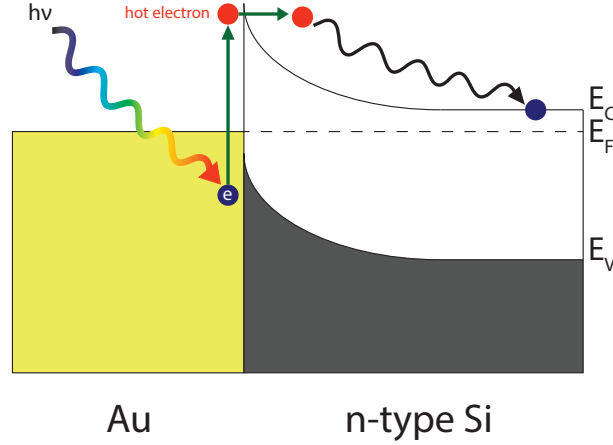
Figure 2.5: Illustration of internal photoemission absorption in Au/n-Si Schottky junction. A photon excites a hot electron which gets injected into the semiconductor and generates photocurrent.

2.2.1 Figures of Merit

Some electrical and optical figures of merit for a photodetector to characterize them will be discussed.

- **Dark current:** Dark current is the DC current flowing through the photodetector in absence of optical signal. Low dark current is of interest for all applications since the optical signals are usually weak signals. So the optical signal will be detectable and signal to noise ratio (SNR) will be high.

- **Photoresponsivity and Quantum Efficiency:** Photoresponsivity is the ratio of photocurrent (I_p) to incident optical power (P_{op}):

$$\mathcal{R} = \frac{I_p}{P_{op}}$$

   At a particular wavelength, in absence of any gain mechanism, there is a maximum limit for the photoresponsivity because at a given optical power, there are limited number of photons that will excite EHPs and contribute to the photocurrent:

$$\mathcal{R}_{max} = \frac{\dfrac{n_e q}{t}}{\dfrac{n_p h\nu}{t}}$$

$$\Rightarrow \mathcal{R}_{max} = \eta \times \frac{q}{h\nu}$$

$$\Rightarrow \mathcal{R}_{max} = \eta \times \frac{q\lambda}{hc}$$

where n_p is the number of incident photons, n_e is the number of photo-generated EHPs, q is the electron charge, and t is time. So the maximum possible photoresponsivity in absence of any gain mechanism is:

$$\mathcal{R}_{max} \simeq \eta \times \frac{\lambda \ (\mu m)}{1.24 \ (\mu m \times \frac{W}{A})} \tag{2.6}$$

where quantum efficiency (η) is defined as the ratio of the number of photogenerated electrons (or holes) to the number of incident photons on the photodetector:

$$\eta \triangleq \frac{n_e}{n_p}$$

Hence, we can derive the quantum efficiency of a photodetector from measurement results:

$$\eta \simeq \frac{1.24 \ (\mu m \times \frac{W}{A}) \times \mathcal{R}}{\lambda \ (\mu m)} \tag{2.7}$$

- **Response Speed:** Response speed of a photodetector is defined as the maximum optical signal frequency that it can detect (not to be mistaken with optical frequency which is the carrier frequency for the optical signal). The response speed of a photodetector depends on carrier transportation time in the device.

2.2.2 PN and PIN Photodiodes

PN and PIN photodetectors can be based on different absorption mechanisms depending on the active material used in them. Photogenerated EHPs within the depletion region of a PN or PIN diode will be extracted by the internal electric field and generate photocurrent. The current in these structures are based on minority carrier diffusion, so these are relatively slow photodetectors. Also PIN photodiode is a faster device compared to PN photodiode due to its longer depletion region resulting in lower depletion capacitance. But long depletion region increases the travel time of the carriers within the device. So the length

of the intrinsic layer of the PIN photodiode should be optimized to achieve the highest operation speed.

2.2.3 Schottky Photodetectors

Metal-semiconductor or Schottky junction photodetectors are hot carrier based photodetectors. Schottky photodiodes are very fast devices since the majority carriers are contributing to the current. Internal photoemission absorption is the main absorption mechanism in sub-bandgap region of this structure.
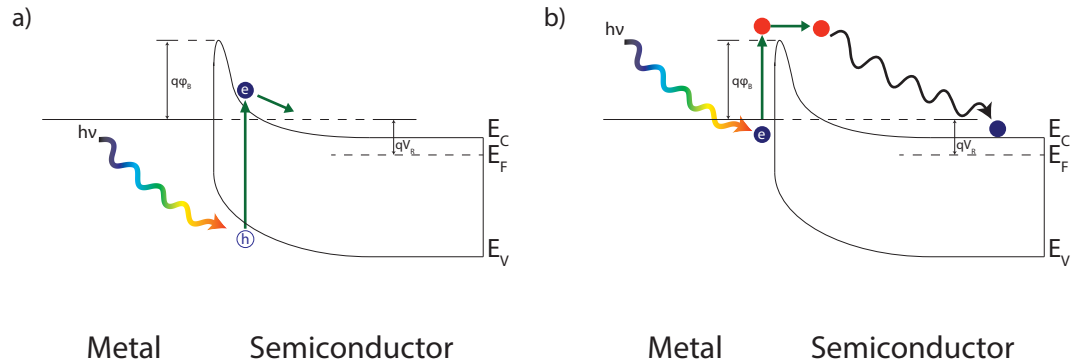
Figure 2.6: (a) Direct absorption and (b) internal photoemission absorption in the Schottky photodetector [29].

2.3 Plasmonics

Plasmonics is the study of light-matter interaction in dimensions comparable or smaller than the wavelength of the light which has gained severe attention recently [25–28, 44–47]. Metals, in traditional electromagnetic theory, behave as perfect conductors since the penetrated electromagnetic waves into the metal are negligible for frequencies up to far-infrared regime. As frequency increases, the penetration of electromagnetic waves into the metal increases and at ultraviolet frequencies, metals behave like dielectrics and allow propagation of electromagnetic waves with attenuation [48]. Electrons in the metal respond to the driving
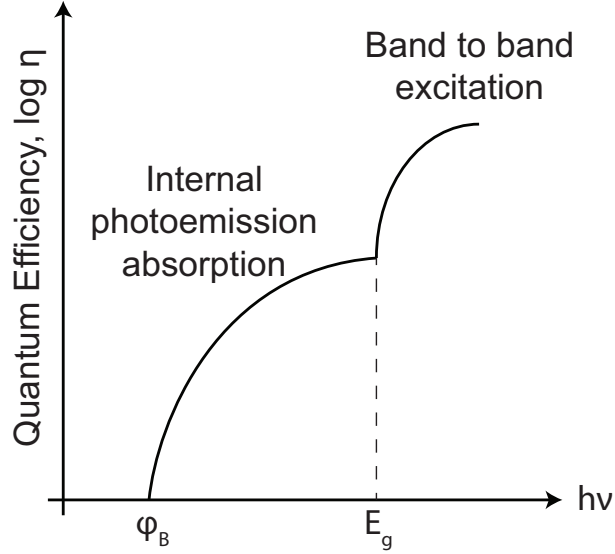
Figure 2.7: Absorption profile of a Schottky photodetector in sub-bandgap regime and direct band to band absorption regime [29].

electromagnetic waves and resonate, which is called plasmon resonances. Also the quanta of these oscillations is called plasmon. Different types of plasmon resonances will be discussed.

2.3.1 Volume Plasmons

In a wide range of frequencies, plasma model for the electrons in the metal can describe the response of the sea of electrons in the metal. Plasma model takes the electron in the metal as free gas moving freely in the metal without taking the electron-electron interactions into account. Writing the oscillator equation for the free electron gas:

$$m\frac{d^2\mathbf{r}}{dt^2} + m\gamma\frac{d\mathbf{r}}{dt} = -e\mathbf{E} \tag{2.8}$$

where m is effective optical mass of each electron, $\mathbf{E} = \mathbf{E}_0 \exp(-j\omega t)$, and $\gamma = \frac{1}{\tau}$ is the collision frequency (τ is the relaxation time of the free electron gas). Solution of this equation is called Drude model since Paul Drude described it at 1900 [49]:

$$\epsilon(\omega) = \epsilon_0(1 - \frac{\omega_p^2}{\omega^2}) \tag{2.9}$$

14

where ω_p is defined as the plasma frequency of the free electron gas in the metal. At frequencies lower than the plasma frequency, the permittivity described in the Drude model is negative leading to imaginary wavenumber $k = \omega\sqrt{\epsilon\mu}$ so the wave will be attenuated and as a result cannot propagate. At frequencies higher than the plasma frequency (plasmonic band), the permittivity will be positive and the metal will act like a dielectric. So the light will penetrate into the metal.

For real metals near the plasma frequency, the Drude model has errors which can be solved by adding the effect of the bound electrons in the d-band of the metal as a damping factor to equation 2.8 and write Drude-Lorentz model to get more predictive results [48, 50].

$$m\frac{d^2\mathbf{r}}{dt^2} + m\gamma\frac{d\mathbf{r}}{dt} + m\omega_0^2\mathbf{r} = -e\mathbf{E} \tag{2.10}$$

where ω_0 is the resonance frequency of the bound electrons. Utilizing the polarization vector for the free electron gas $\mathbf{P} = -ne\mathbf{r}$ [48] and assuming a possible result for $\mathbf{P}$ like $\mathbf{P}_0\exp(-j\omega t)$ we can solve the equation:

$$\mathbf{P} = \frac{ne^2}{m(\omega_0^2 - \omega^2 - j\gamma\omega)}\mathbf{E} \tag{2.11}$$

Using the permittivity $\epsilon = 1+\chi$ and dielectric susceptibility $\mathbf{P} = \epsilon_0\chi\mathbf{E}$ definitions, we can write:

$$\epsilon(\omega) = 1 + \frac{\mathbf{P}}{\epsilon_0\mathbf{E}} = 1 - \frac{\omega_p^2}{\omega_0^2 - \omega^2 - j\gamma\omega} \tag{2.12}$$

where $\omega_p \triangleq \frac{ne^2}{\epsilon_0 m}$ is defined as the plasma frequency of the free electron gas in the metal. Hence we can derive the real and imaginary parts of the permittivity:

$$\epsilon_1(\omega) = 1 + \frac{\omega_p^2(\omega_0^2 - \omega^2)}{(\omega_0^2 - \omega^2)^2 + \gamma^2\omega^2} \tag{2.13a}$$

$$\epsilon_2(\omega) = \frac{\omega_p^2\gamma\omega}{(\omega_0^2 - \omega^2)^2 + \gamma^2\omega^2} \tag{2.13b}$$

2.3.2   Surface Plasmons

Surface plasmon polaritons (SPP) are propagating surface waves at a metal-dielectric interface as a result of coupling of the oscillation of the electrons in the

15

metal with incident electromagnetic waves. A complete solution of the Maxwell's equations is required for fully understanding the genesis of these waves as well as methods of excitation of SPPs. Solving the Maxwell's equations for TM and TE modes of a propagating wave in the metal-dielectric interface (Fig. 2.8), reveals that the TE SPPs do not exist and TM SPPs require:
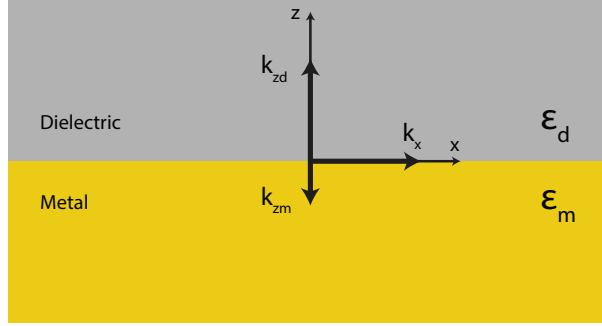
Figure 2.8: Wave vectors in the metal-dielectric interface.

$$\frac{k_{zm}}{k_{zd}} = -\frac{\epsilon_m}{\epsilon_d} \qquad (2.14)$$

where k_x is the wave vector component of the propagating surface plasmon in x-direction, ϵ_d is permittivity of the dielectric, ϵ_m is permittivity of the metal, and k_{zd} and k_{zm} are the components of the dielectric and metal wave vectors in z-direction, respectively. From equation 2.14 we can infer that for a SPP to propagate, a metal (with negative $\Re[\epsilon]$) and a dielectric should be in contact. Dispersion relation of the SPP at the metal-dielectric interface is shown in Fig. 2.9. From the dispersion curves, it is obvious that without a special excitation setup, light coming from the dielectric is not able to excite a SPP due to k-vector mismatch. For a SPP to propagate, excitation setups like gratings [51], Kretschmann [52], and Otto [53] are required.

2.3.3 Localized Surface Plasmons

Metal nanoparticles can excite non-propagating SPP modes in the metal-dielectric interface which are called localized surface plasmons. Unlike the propagating SPPs, localized SPPs can be excited under illumination without the need

16
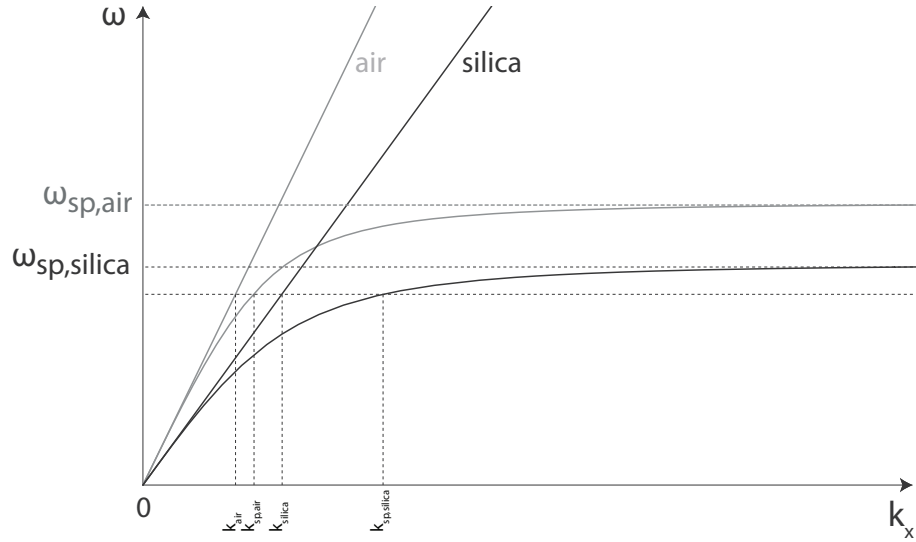
Figure 2.9: Dispersion relation of the air and silica with real part of the SPP dispersion relation in the contact of a metal with air and silica [48].

to any matching setup. For obtaining a consistent solution for nanoparticles under illumination, we can start from infinitesimal nanoparticles which are very smaller than the light wavelength. So we can take the E-field uniform through the nanoparticle. This is known as quasi-static approximation. Solving for the effect of a time-varying electric field uniform over a nanoparticle (Fig 2.10):
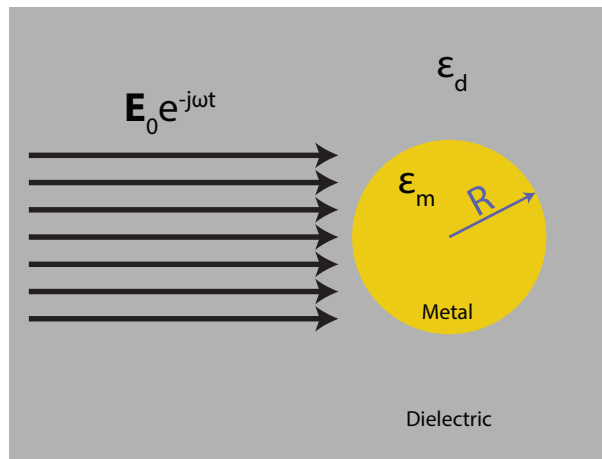
Figure 2.10: Nanoparticle under illumination. Electric field is constant near the nanoparticle (quasi-static approximation).

$$\mathbf{E}_i = \frac{3\epsilon_d}{\epsilon_m + 2\epsilon_d} \mathbf{E}_0 \exp(-j\omega t) \qquad (2.15)$$

17

Quasi-static approximation results in an induced dipole with momentum P:

$$\mathbf{P}_i = R^3 \frac{\epsilon_m - \epsilon_d}{\epsilon_m + 2\epsilon_d} \mathbf{E}_0 \exp(-j\omega t) \tag{2.16}$$

We can see that the polarizability experiences a resonance when:

$$\Re[\epsilon_m] = -2\epsilon_d \tag{2.17}$$

This is called Frölich condition [48] at which the nanoparticle will experience a peak in its dipole momentum. So the metal nanoparticle will concentrate the light to its vicinity and increase the absorption significantly. Also it can increase the absorption in its near-field region if it is surrounded by an absorbing material. From the equation 2.17 we can infer that the resonance peak position in the frequency spectrum is highly dependent on the surrounding dielectric. Increasing the permittivity of the dielectric results in a red-shift in the nanoparticle plasmon resonance. Also the plasmon resonance depends on the nanoparticle size [54]. Decreasing the size of the nanoparticle increases the collisions of the oscillating electrons from the surface [55]. Effect of the particle size on the resonance frequency of very small particles ($R < 10\ nm$) can be modelled in vacuum surrounding which gives an insight into the problem [55–59]:

$$\omega_s = \frac{A\nu_F}{R} \tag{2.18}$$

where ω_s is the peak frequency of the plasmon resonances, A is a proportionality factor in the order of unity, ν_F is the Fermi velocity ($\nu_F = 1.4 \times 10^{-14}\ cm/s$ for gold and silver [58]), and R is the radius of the nanoparticle. Also size effect of larger particles beyond the quasi-static approximation is studied [60, 61]. The expansion of the first TM mode of Mie theory [48, 62] results in:

$$\mathbf{P}_i = V \frac{1 - \dfrac{\epsilon_m + \epsilon_d}{10} x^2 + O(x^4)}{\dfrac{1}{3} + \dfrac{\epsilon_m}{\epsilon_d - \epsilon_m} - \dfrac{\epsilon_d + 10\epsilon_m}{30} x^2 - j \dfrac{4\pi \epsilon_m^{\frac{3}{2}} V}{3\lambda_0^3} + O(x^4)} \mathbf{E}_0 \exp(-j\omega t) \tag{2.19}$$

where V is the particle volume, and $x \triangleq \dfrac{\pi R}{\lambda_0}$ is defined as size parameter. Also the quadratic expressions in the equations model the retardation of exciting and depolarization fields [60]. The results for both regimes shows that bigger nanoparticles resonate at longer wavelengths, so increasing the nanoparticle size causes a red-shift in the plasmon resonance.

Surface plasmon polaritons are a way to localize the electromagnetic waves by carefully designing the plasmonic nanoparticles, giving a boost to light trapping and increasing the efficiency of optoelectronic devices like solar cells, subsequently. In 1970s, it was shown that plasmons can decay via a radiative (emitting photons) [63] or a non-radiative (exciting hot carriers) procedure [64]. These competing decay processes are dependent on the size and shape of the plasmonic structure. Plasmon resonances in larger particles are prone to lose their energy to photons, decreasing the strength of the resonance and as a result, decreasing the absorption [65, 66].

Chapter 3

Fabrication Techniques

We used the ISO 5 (class 100) and ISO 6 (class 1000) cleanrooms in National Nanotechnology Research Center (UNAM) of Bilkent University for the fabrication steps. In this chapter, the fabrication techniques as well as the recipes for each step of the study will be introduced and discussed. Then the fabricated photodetectors with full recipe and SEM images will be presented.

3.1 Fabrication Techniques and Recipes

3.1.1 Wafer Selection, Dicing, and Cleaning Procedure

We have used 4-inch lowly doped n-type (100) Silicon wafers with resistivity of $2 - 5$ $^{\Omega-cm}$ throughout this study. The wafers were diced into $15mm \times 15mm$ dies for fabricating a photodetector sample (Fig. 3.1). Then, 2 consecutive steps of cleaning were done on every die just before the sample fabrication.

First step is making a Piranha solution. Piranha solution is the mixture of Sulphuric acid (H_2SO_4) to Hydrogen peroxide (H_2O_2) which removes organic contaminations. Also due to its oxidizing nature, a thin SiO_2 layer will be formed
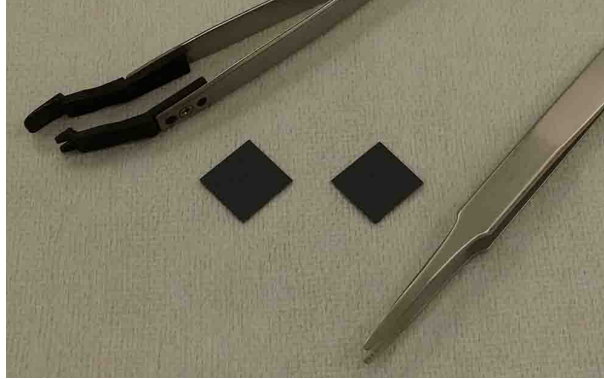
Figure 3.1: Diced Silicon wafers.

on Silicon after cleaning with Piranha solution, which makes the surface of the die hydrophilic. In this step we dipped the dies into a solution of (4:1) H_2SO_4 to H_2O_2 for 5 minutes on a hot plate at 80°C and rinsed them with deionized (DI) water.

Second step of cleaning process is removing the oxide layer formed in Piranha etching step. Buffered oxide etch (BOE or BHF) was used for approximately 30 s until observing hydrophobic behavior followed by rinsing with DI water and drying with N_2 gun.

3.1.2   Metal Deposition

We used Ag and Au as metal contacts of our Schottky photodetectors. Thermal evaporation technique was used for depositing Ag using VAKSİS Thermal Evaporation (Fig 3.2) and sputtering technique was used for depositing Au using Gatan, Inc. Precision Etching Coating System (PECS) (Fig 3.3).

3.1.3   Photolithography

Using EVG® 620 Mask Alignment System (Fig. 3.4), we can resolve features down to 2 μm in size by photolithography technique. Photolithography was used

Figure 3.2: VAKSİS Thermal Evaporation system.

for patterning the Al-doped Zinc Oxide layer.

- **Photoresist Deposition:** AZ5214 photoresist was spin-coated on the samples before photolithography. Parameters of the spin-coating is in Table. 3.1.

Time	Acceleration	Speed
50 s	1000 rpm/s	5000 rpm

Table 3.1: Spin-coating parameters

- **Pre-bake:** The dies were baked at 110°C on hot plate for 1 minute.

- **First Exposure:** Exposure was done with 40 mJ/cm^2 of UV light dose with the mask containing the photodetector patterns for resolving the patterns on the photoresist coated dies.

- **Image Reversal Bake:** Then 2 minutes of baking at 120°C on hot plate was done for doing an image reversal photolithography.

- **Second Exposure:** Exposure was done with 160 mJ/cm^2 of UV light dose without a mask for completing the image reversal photolithography.

Figure 3.3: Gatan, Inc. Precision Etching Coating System (PECS).

Figure 3.4: EVG® 620 Mask Alignment System.

- **Developing:** After photolithography, dies were developed in a solution of (4:1) DI water to AZ 400K for approximately 50 s until removal of photoresist.

- **Inspection under Microscope:** Then the patterned dies were inspected under a microscope to see if the photolithography was successful or not (Fig. 3.5).

- **Removing the Photoresist:** Finally, the photoresist was cleaned from the dies using Acetone, followed by dipping into Isopropyl Alcohol (IPA or Isopropanol). Then the dies were rinsed with DI water and cleaned by N_2 gun.
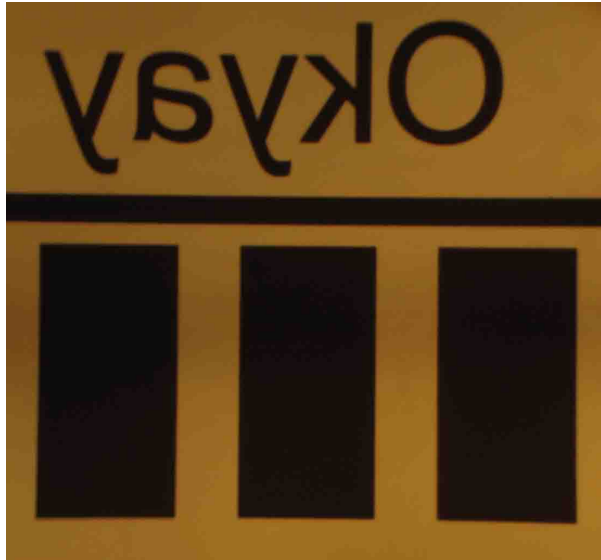
Figure 3.5: Microscope image of a photodetector right after photolithography and development steps.

3.1.4 Lift-off

A thin metal film can be patterned by depositing the metal on a pre-patterned photoresist (or e-beam resist) and dissolving the resist in a solvent like Acetone ($(CH_3)_2CO$) (Fig. 3.6). We have used this method during device fabrication using e-beam lithography.
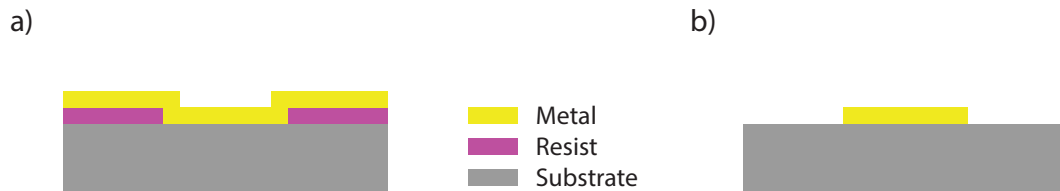
Figure 3.6: Depiction of the lift-off process. (a) Metal deposition on a pre-patterned resist film. (b) Peeling off the resist using a solvent.

3.1.5 Forming Metal Nanoislands by Rapid Thermal Process

Rapid thermal annealing (RTA) of thin metallic layer creates metal nanoislands and the average size of the nanoislands depend on the RTA temperature [43, 67] (Fig. 3.7). Since this method is ultra-low-cost and easily results in random sized and randomly distributed nanoislands, we chose this technique in order to make plasmonic nanoparticles. This method gives a good control over the average size of the nanoislands which determines the resonance spectrum. Also there are higher and lower limits for the annealing temperature. Very low annealing temperatures result in connected particles and high temperatures are limited to RTA tool's higher limit or the melting point of the metal. In this study we have used SRO-704 RTA system from ATV Technologie GmbH (Fig.3.8) with a sample recipe explained in Table. 3.2.
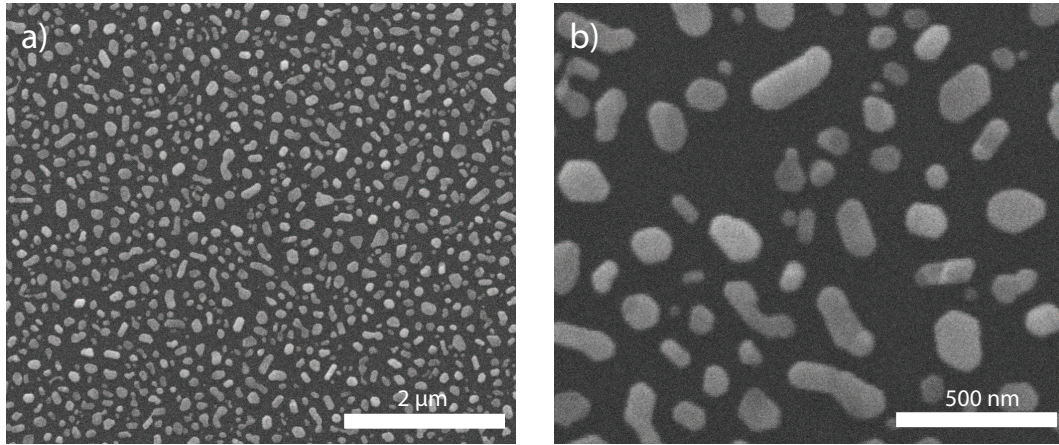
Figure 3.7: SEM image of metallic nanoislands formed using RTA.

Step	Duration	Temperature
1	30 s	0 to 450°
2	60 s	450°
3	5 s	450° to 0

Table 3.2: RTA recipe (setpoint temperature is 450° and no cooling system was used).

Figure 3.8: ATV Technologie GmbH, SRO-704 RTA system.

3.1.6 Atomic Layer Deposition

Atomic Layer Deposition (ALD) is special chemical vapor deposition (CVD) technique in which the reactions are formed on the sample surface and are separated in time. Every reaction has a self-limiting nature, so consecutive reactions in the chamber lets us control the film thickness, monolayer by monolayer. The reactions for deposition of an Al_2O_3 monolayer are [29]:

$$OH \cdot Si + Al(CH_3)_3 \rightarrow AlO(CH_3)_2 \cdot Si + CH_4$$
$$AlO(CH_3)_2 \cdot Si + 2H_2O \rightarrow AlO(OH)_2 \cdot Si + 2CH_4$$
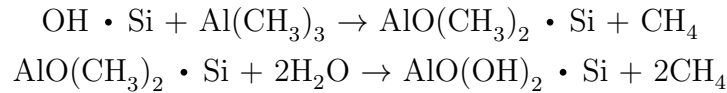
We have used Cambridge Nanotech Inc., Savannah S100 ALD system (Fig. 3.9) to deposit Aluminum-doped Zinc Oxide (AZO) film. ZnO is a transparent semiconductor due to its large bandgap (3.3 eV). Doping ZnO with Al makes it very conductive and can be used as a transparent contact to connect the nanoislands electrically while it allows light to penetrate into the structure (transparent conductive oxide or TCO). Also AZO forms a heterojunction with Silicon [68] which causes a diode-like I-V characteristics in the reference sample (AZO reference) which will be discussed in Section 4.2.2. The AZO recipe contains 16 supercycles followed by 28 cycles of ZnO at the end of the recipe. Each supercycle is consisted of 28 cycles of ZnO followed by 1 cycle of Al_2O_3. The deposition temperature was 250°C. The detailed parameters of the ALD recipe is explained in Table. A.1.

Figure 3.9: Cambridge Nanotech Inc., Savannah S100 ALD system.

3.2 Device Fabrication Steps

Nanoisland formation using RTA was used for fabrication of photodetectors (Fig. 3.10). A recipe for fabrication of a photodetector will be described (the methods are introduced before in details):

- Die cleaning using Piranha solution and BOE.

- Deposition of 10 nm of Au using PECS or Ag using thermal evaporation.

- Rapid thermal annealing the dies for different temperatures: 300°C, 450°C, 600°C.

- Deposition of approximately 50 nm of AZO using ALD.

- Photolithography and creating 600 $\mu m \times$ 300 μm rectangular patterns on AZO layer.

- Wet etching of the AZO using Nitric acid (HNO_3) for exactly 8 seconds. Since HNO_3 can etch Ag and also damages the photoresist in approximately 12 seconds, this step should be carefully done.

- Removing the photoresist using Acetone and IPA.

- Rinsing with DI water.
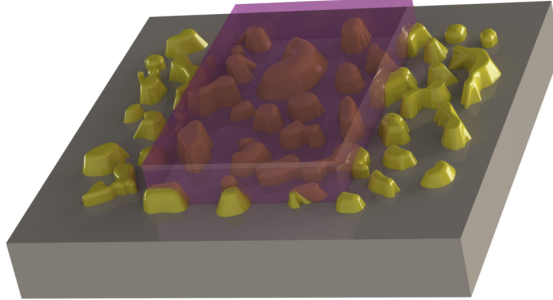
Figure 3.10: Depiction of the fabricated photodetectors [43].

3.2.1 Ag Nanoislands

Two samples were fabricated with Ag nanoislands at 300°C (Fig. 3.11) and 600°C (Fig. 3.12). Since the plasma frequency of the Ag is in visible region [69], the Ag nanoislands did not resonate at sub-bandgap regime of Silicon. Due to the size limitation of the RTA method, the resonance spectrum of the Ag nanoislands were not extended into the NIR region by increasing the average nanoisland size. So Ag nanoislands were not suitable for photodetector fabrication with the RTA method.
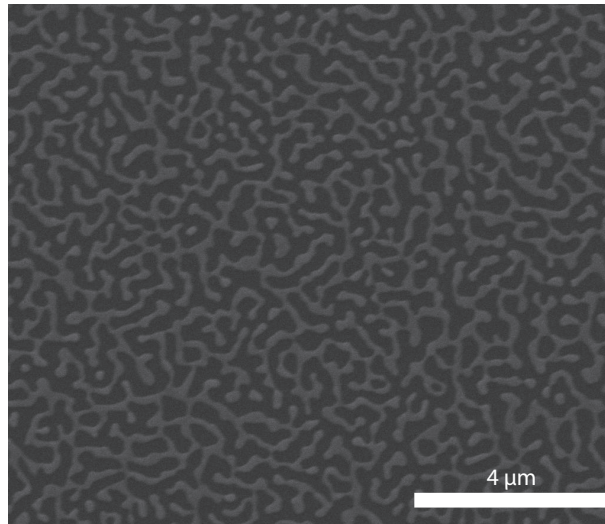
Figure 3.11: SEM image of Ag nanoislands formed at 300°C.
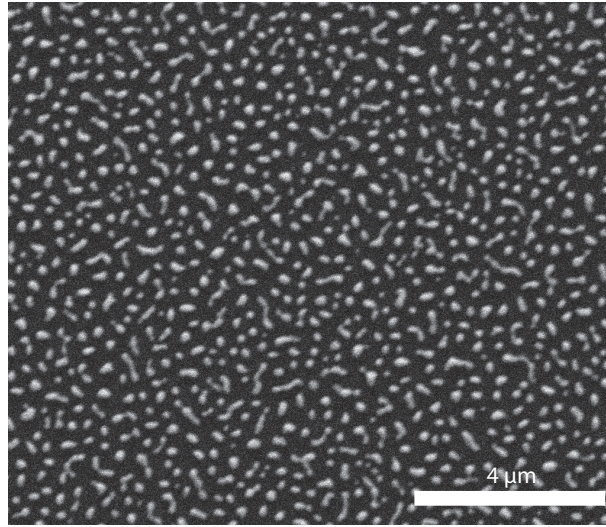
Figure 3.12: SEM image of Ag nanoislands formed at 600°C.

3.2.2 Au Nanoislands

It is known that Au has a plasma frequency in the NIR region. We fabricated Au nanoislands at 300°C (Fig. 3.13), 450°C (Fig. 3.14), and 600°C (Fig. 3.15). Using ImageJ software, we processed the SEM images to find the boundaries of the nanoislands and counted them. Then using MATLAB®, we processed the data extracted form image processing procedure and plotted the particle size histograms.
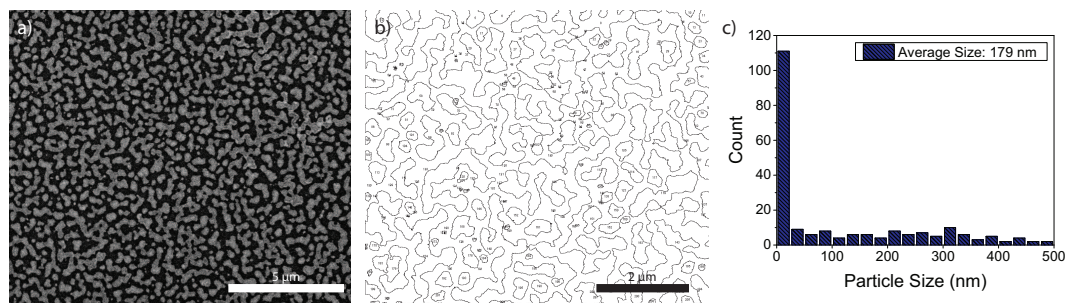
Figure 3.13: (a) SEM image, (b) processed image, and (c) particle size histogram of Au nanoislands formed at 300°C. The average particle size is 179 nm.
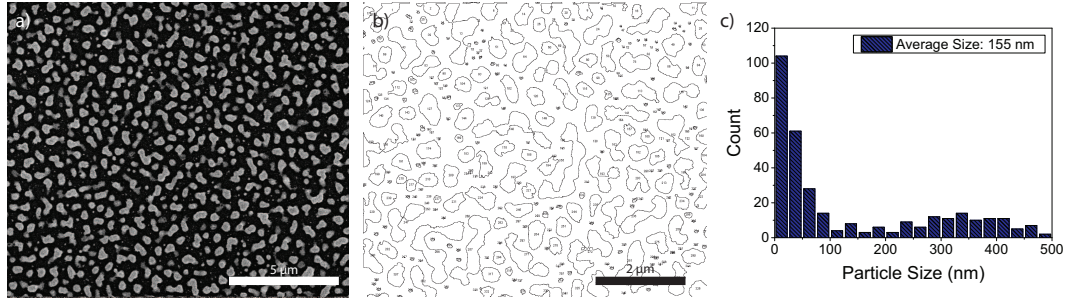
Figure 3.14: (a) SEM image, (b) processed image, and (c) particle size histogram of Au nanoislands formed at 450°C. The average particle size is 155 nm.
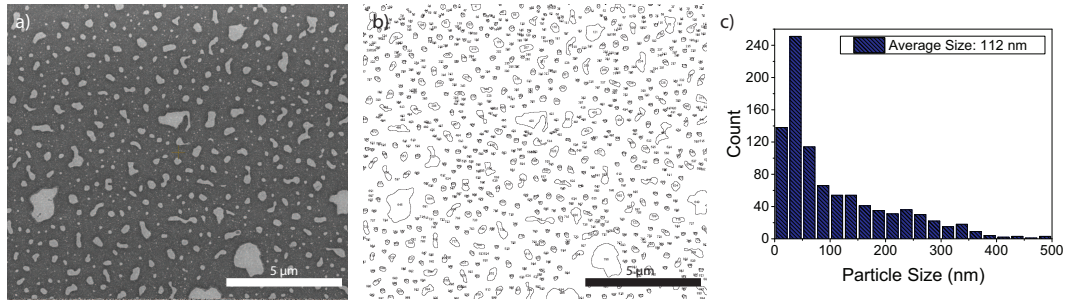
Figure 3.15: (a) SEM image, (b) processed image, and (c) particle size histogram of Au nanoislands formed at 600°C. The average particle size is 112 nm.

According to Figures 3.13-3.15, the particle sizes are strongly dependent on temperature of the annealing step. Nanoislands formed at 300°C are like semi-continuous metal film with highest average particle size. Increasing the annealing temperature to 450°C and 600°C segregates the nanoislands and decreases the average particle size. As we discussed in Section 2.3.3, we expect stronger resonance in longer wavelengths for the photodetector annealed at 300°C, due to its larger average particle size.

Chapter 4

Simulation and Characterization

In this chapter, 2D and 3D simulation and measured results will be provided and discussed. We simulated nanoparticles of Al, Ag, and Au and then fabricated some of the promising devices.

4.1 FDTD Simulations

Finite Difference Time Domain (FDTD) is a numerical method for solving Maxwell's equations. We used Lumerical FDTD software, which is a CAD tool for FDTD simulations, in order to calculate the absorption spectra of the metal nanoparticles.

4.1.1 Al and Ag Nanoislands

We simulated the absorption spectra of periodically distributed identical nanoparticles of these metals with periodicity of 1000 nm surrounded by AZO layer as the electrical contact (Fig. 4.1). The optical constants of AZO was extracted using J.A. Woollam Co. Inc. VASE ellipsometer (Appendix B) and that of

the Silicon and the metals was imported from existing experimental data in the literature [70, 71].
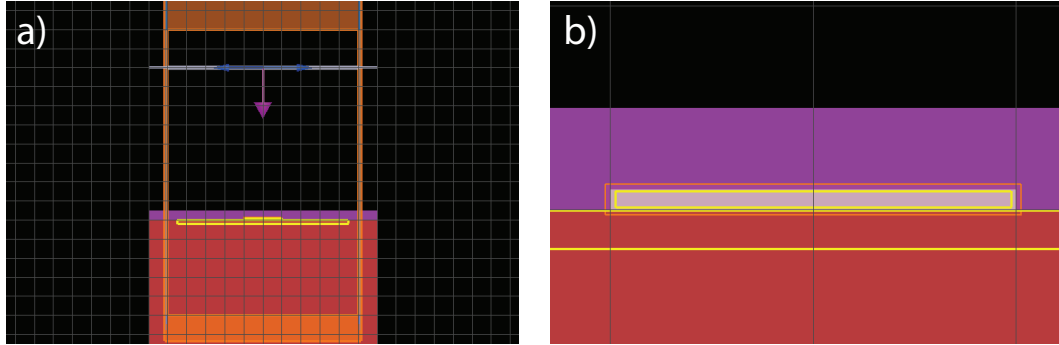
Figure 4.1: Simulation setup for nanoparticles. The metal is on the Silicon substrate and buried under AZO layer.

According to our 2D simulations (Figures 4.2 and 4.3), Al and Ag nanoparticles exhibit resonance in visible region which is in agreement with the literature [46, 47, 72]. The plasma frequency of Al and Ag are in visible region making it difficult to shift the resonance frequency of them into the NIR. Also we cannot change the metal thickness and size beyond some limits due to the nature of RTA method (thicker metal films does not form nanoislands and formation of larger nanoparticles are not possible by simple decreasing the annealing temperature). Hence, it was not possible to fabricate Al and Ag nanoislands with average particle sizes larger than 200 nm with RTA method. For that reason, Al and Ag nanoislands did not resonate in NIR region and are not suitable materials for light absorption in our photodetectors.
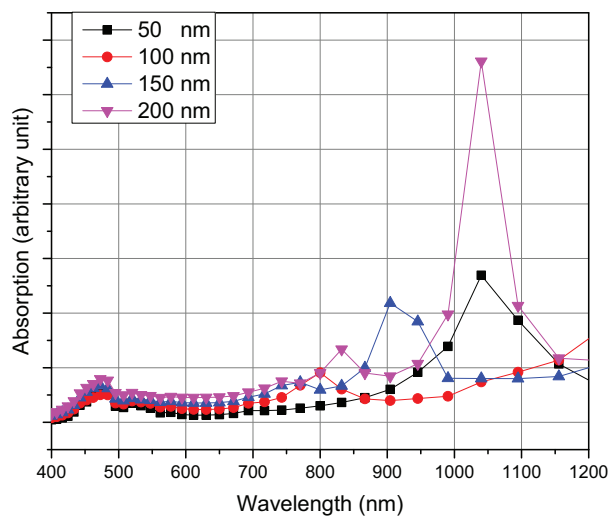
Figure 4.2: Absorption spectrum for Ag nanoparticles with different sizes.
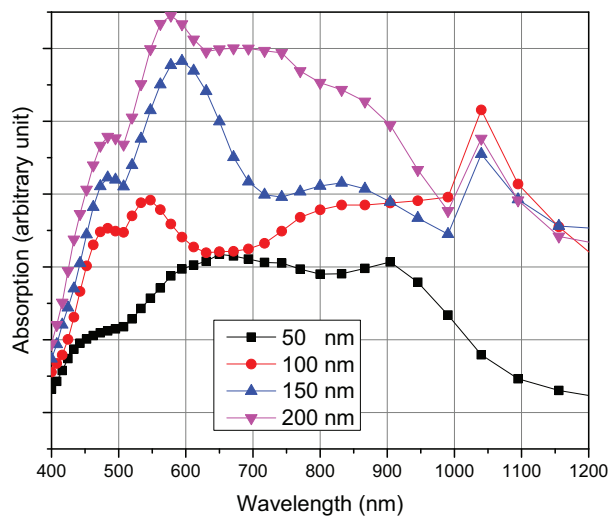
Figure 4.3: Absorption spectrum for Al nanoparticles with different sizes.

4.1.2 Au Nanoislands

Au nanoislands had promising results in the simulations. Au has lower plasma frequency than Ag and Al [69]. Therefore, Au resonates at higher wavelengths leading to enhancement of the electric field in NIR region. The resonance of Au nanoparticles red-shift as we increase the size (Fig. 4.4). So a very thin Au nanoisland layer seemed propitious for an ultra-low-cost NIR photodetector (Fig. 4.4(b)). Photodetectors with thicker Au films are studied in the literature [27] showing the frequency shift of the narrowband absorption spectrum of the grating-based photodetectors with changing the grating width (Fig. 4.5).
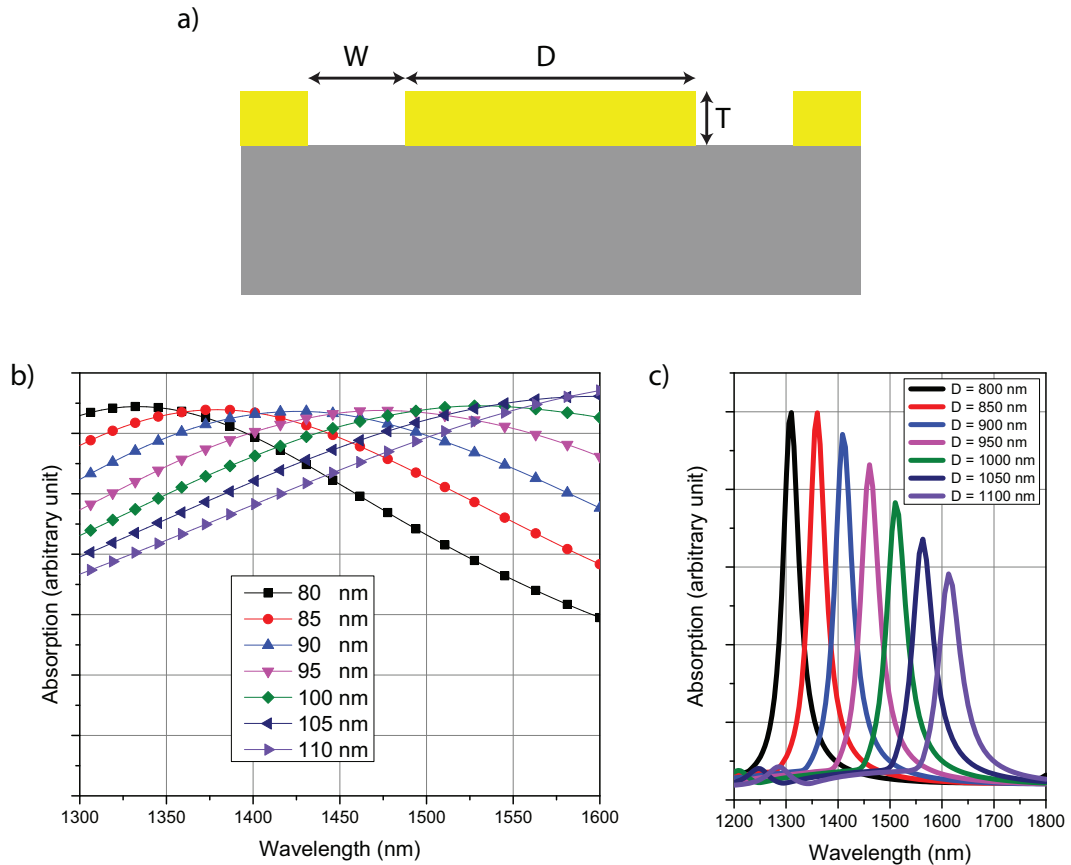
Figure 4.4: a) Illustration of the simulation parameters. Absorption spectra of Au nanoparticles with different sizes are shown. b) $T = 10\ nm$ and $W = 1000\ nm$. D is swept between 80 nm and 110 nm. c) $T = 200\ nm$ and $W = 250\ nm$. D is swept from 800 nm to 1100 nm. The absorption profile red-shifts with increasing the nanoparticle size
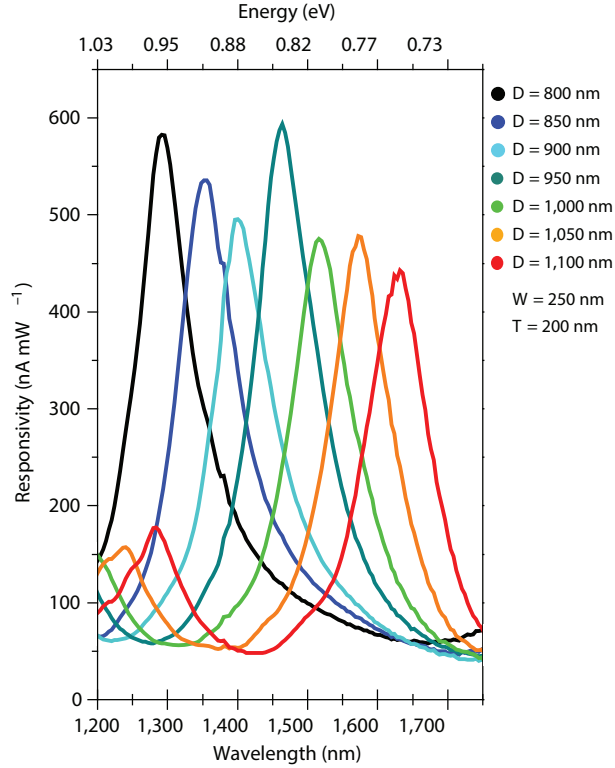
Figure 4.5: Responsivity curves of the Au gratings on Silicon photodetectors showing the red-shift with increasing the grating width [27].

Using RTA method we fabricated Au nanoislands on Silicon and simulated the actual 3D model of the fabricated samples by importing the processed SEM image of the samples into FDTD simulation environment and extruded them 10 nm (Fig. 4.6). This 3D model is an approximate model since we have not imported the height information of the particles. Also sharp edges are the artefacts of extruding the SEM images which are not the case in actual nanoislands. Nevertheless, our results (Fig. 4.7) are in good agreement with the measurement results (Section 4.2).
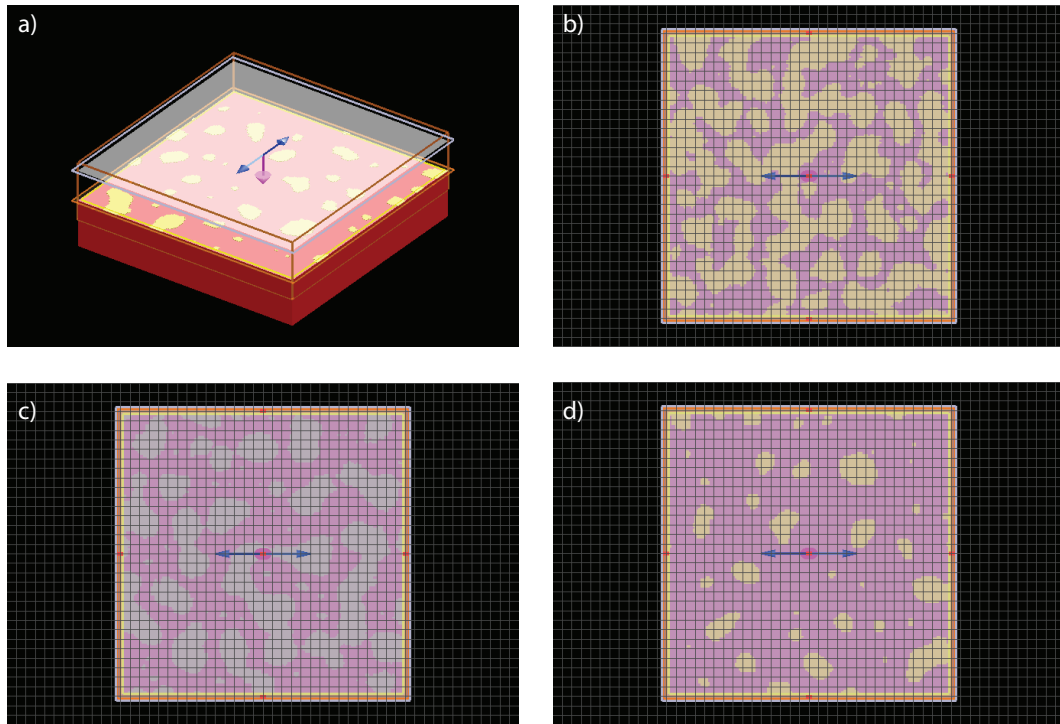
Figure 4.6: (a) Perspective view of the FDTD 3D simulation setup. Top-view of the sample annealed at (b) 300°C, (c) 450°C, and (d) 600°C
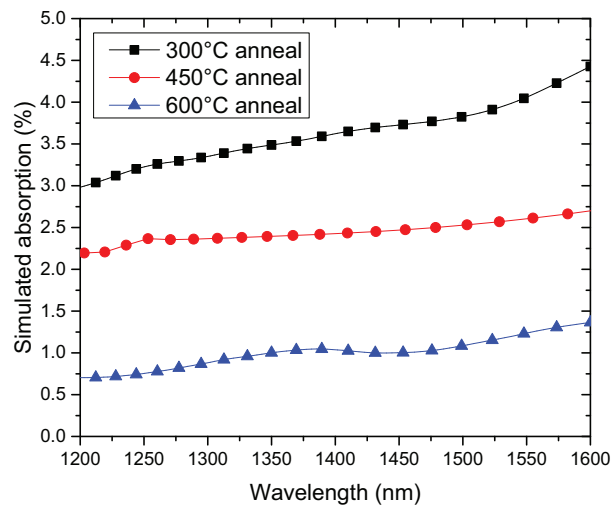
Figure 4.7: Simulated absorption profile of the photodetectors with Au nanois-lands.

4.2 Characterization and Measurement Results

This section provides information about characterization methods and tools that we designed and used during this study as well as the measurement results of the fabricated photodetectors.

4.2.1 Characterization Setup

For characterization of broad-band photodetectors, we needed a broad-band laser setup that have control on the output wavelength and polarization. Using a Fianium Ltd, supercontinuum laser source (WL-SC400-2) which provides white light from 390 nm to 2400 nm, we could design an automatic spectral photoresponsivity measurement system which provides two channels of laser using a custom designed optical path. One from 600 nm to 1150 nm and the other from 1100 nm to 2000 nm. Due to limitations in measurement of output power, we are able to measure the photocurrent up to 2000 nm, but the photoresponsivity is limited to 1600 nm.
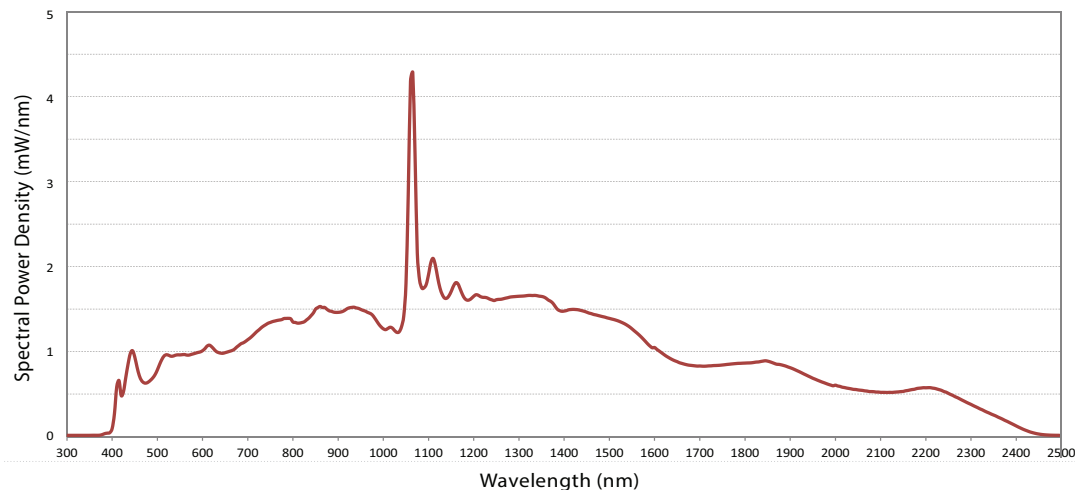
Figure 4.8: Spectral power density of the supercontinuum laser source used in the characterization setup.

The output of laser feeds a two-channel Fianium Ltd, acousto-optic tunable filter (AOTF). The AOTF gets the white laser beam as input and gives a quasi-monochromatic output laser filtered at the given wavelength. The output laser goes through an optical path with polarization control mechanism and a mechanical chopper. Then using a 20x objective lens we shine the laser normally on the photodetector with a beam waist of approximately 50 μm. Then, the photodetector is probed with micromanipulators and sit in an electrical circuit which includes a KEITHLEY 2401 Sourcemeter and a Stanford Research Systems SRS830, lock-in amplifier. The sourcemeter biases the photodetector and the lock-in amplifier reads the photocurrent by adaptively filtering the input current with a feedback from the rotation speed of the mechanical chopper in order to suppress the effect of noise and ambient light. The measurement tool is controlled using software written in LabVIEW® (Fig. 4.10). The image of the measurement tool is shown in Fig. 4.9.
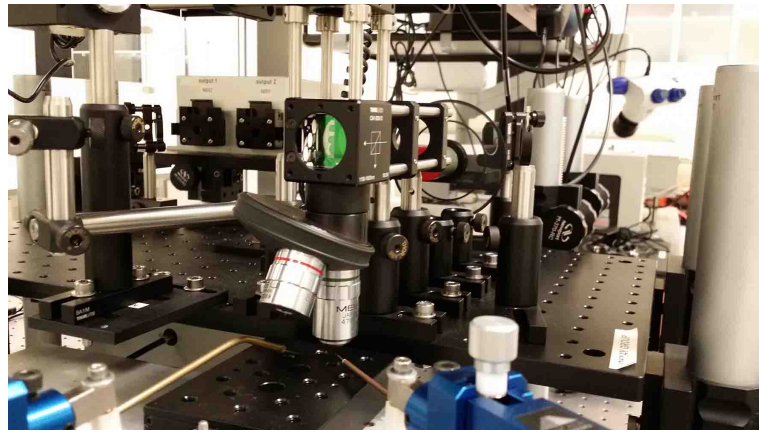
Figure 4.9: Spectral photoresponsivity measurement tool in our lab.
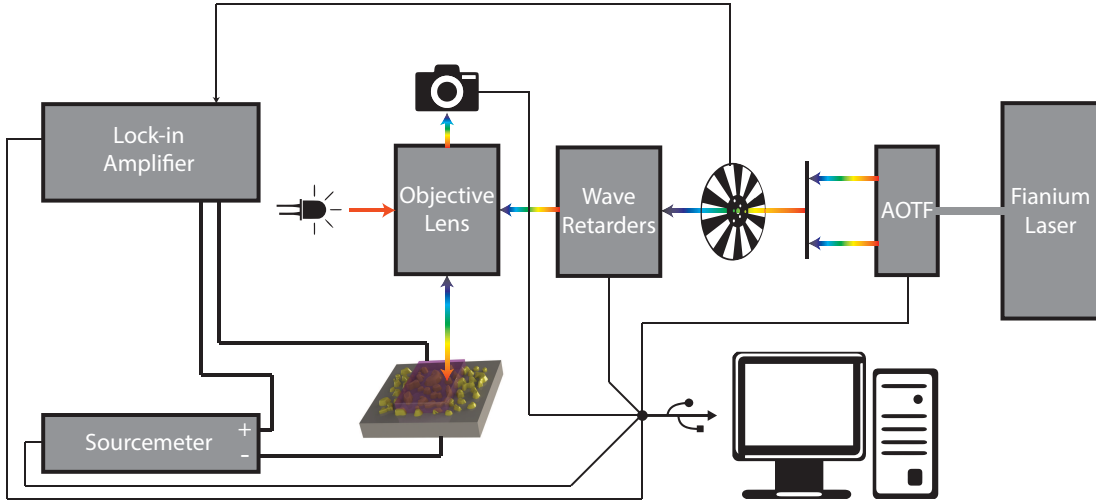
Figure 4.10: Schematic of the spectral photoresponsivity measurement setup.

4.2.2 Measurement Results

The I-V measurement in dark condition (Fig. 4.11) and photoresponsivity results (Fig. 4.12) for Au nanoislands will be presented.

We fabricated two reference devices. In the first reference, we skipped the metal deposition and RTA steps. So it does not have metal nanoislands between AZO and Silicon (AZO reference). This was for understanding the behavior of AZO layer. In the other reference, we formed 10 nm thick Au film and patterned it with 300 $\mu m \times 600\ \mu m$ rectangles using lift-off method (Section 3.1.4) which was for understanding the effect of nanoparticles vs. planar metal film (Au reference). We expected that the AZO reference will not absorb light and will be transparent in NIR region. Also for Au reference we expected very low photoresponsivities since direct illuminated light will not be able to excite surface plasmons in a large pad of Au.

According to the Fig. 4.11, the dark current density is calculated at $-1\ V$ for all the samples (Table. 4.1). The reported dark current densities are considered as very low compared to the literature values of Silicon photodetectors.

39
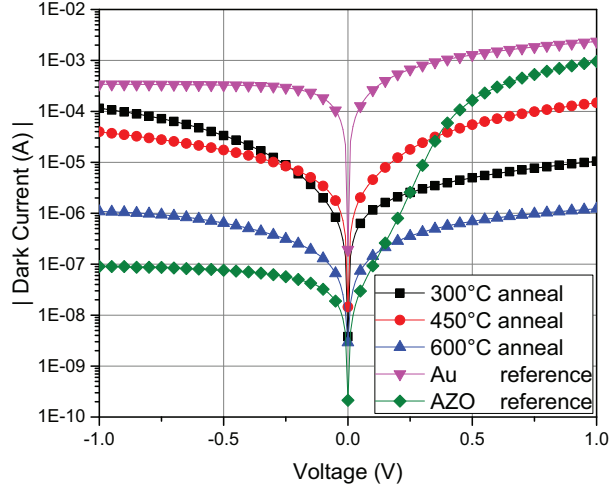
Figure 4.11: IV characteristics of Au nanoislands annealed at different temperature as well as the two reference samples [43].

	300°C	**450°**C	**600°**C
$\mathbf{J_{dark}}$ (mA/cm^2)	63.8131	22.0879	0.6038

Table 4.1: Dark current of the nanoislands samples. The area of the devices are 1.8×10^{-3} cm^2.

During the photoresponsivity measurements, we noticed relatively high photocurrents even at 2000 nm wavelength which is astounding for a Silicon-based photodetector, but we could not measure the photoresponsivity beyond 1600 nm. The photocurrent measured at 2000 nm wavelength was in the same order of the photocurrent at 1600 nm. According to the decreasing of the output power of our laser source after 1600 nm (Fig. 4.8), the photocurrent which was measured at 2000 nm was relatively high, considering the fact that the energy of the photons are very low at longer wavelengths.
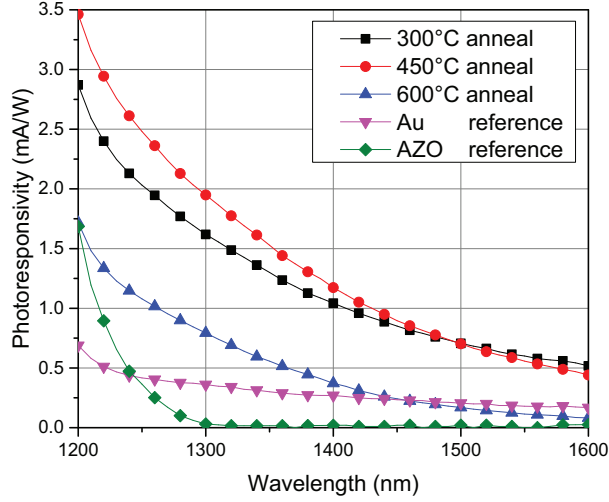
Figure 4.12: Measured photoresponsivity of the Au nanoisland samples and the references [43].

4.2.3 Discussion

We calculate the photoresponsivities of the Au nanoisland samples using the simulated absorption profiles. For a given photodetector, we processed its SEM image and imported that to the FDTD environment and extruded the binary images by 10 nm (Fig. 4.6). Solving for the absorption profile, we extracted the absorption spectrum of the photodetector (Fig. 4.7). This absorption profile indicates the ratio of the absorbed photons to the total incident photons. Assuming that every absorbed photon excites a hot-electron and considering no other wavelength dependent factor, we used the Fowler model (Eqn. 2.4) for IPE photodetection. For calculating the total quantum efficiency of the photodetector we multiplied the absorption profile by the Fowler function. Then we fit the result with the measured photoresponsivity data and extracted the Fowler coefficient and Schottky barrier height for each device independently. Without surprise, the extracted Schottky barrier height ($\phi_b \simeq 0.7 \ eV$) from our IPE photodetection model, was expected from Au-Si Schottky junctions [29]. The extracted Fowler coefficients are provided in Table 4.2.

	300°C	**450°**C	**600°**C
$\mathbf{C_F}$	3.8×10^{21}	7.8×10^{21}	3.5×10^{21}

Table 4.2: The extracted Fowler coefficients for the Au nanoisland samples annealed at different temperatures.
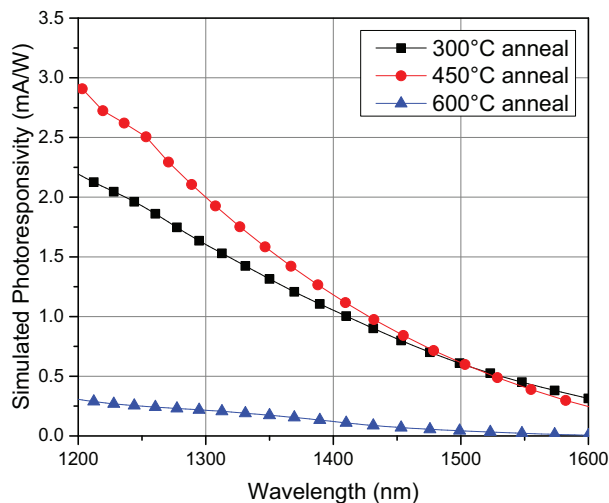
Figure 4.13: Simulated photoresponsivity of the Au nanoisland samples [43].

Using the extracted properties, we plotted the simulated photoresponsivity curves for the Au nanoisland photodetectors (Fig. 4.13). According to the experimental (Fig. 4.12) and simulated (Fig. 4.13) photoresponsivity results, the hot-electron based photodetection from experimental results, which occurs after the effects of absorption tail of the Silicon, is perfectly matching with the simulated results (approximately > 1300 nm). But since we have not considered the effect of the absorption tail of the Silicon after its cut-off wavelength ($\lambda_C \simeq 1100$ nm), in wavelengths below 1300 nm, the simulated photoresponsivity curves experience a small drop compared to the experimental results. In that part of the spectrum, Silicon has an extensively vanishing absorption behavior which is enhanced by light concentration in Silicon surface near the metal nanoislands due to localized plasmon resonances in metallic nanoparticles. So this absorption is not negligible anymore and have to be considered for all these photodetectors. Hence, for more accurate simulations one has to consider the absorption in the depletion region of the Silicon as well.

As we discussed in Section 2.3.3, larger particles resonate at longer wavelengths. So according to the particle size histograms (Fig. 3.13(c), Fig. 3.14(c), and Fig. 3.15(c)), the photodetector which is annealed at 300°C should show higher photoresponsivities at longer wavelengths than the photodetector annealed at 450°C, which is in strong agreement with both experimental and simulated results. Also the crossover point of the photoresponsivity curves of these two samples (at 1500 nm) was estimated using the simulations. This crossover point is due to the fact that the photodetector annealed at 300°C is effectively absorbing longer wavelengths compared to the sample annealed at 450°C and at this point its photoresponsivity is surpassing that of the sample annealed at 450°C. Also, the sample annealed at 600°C has smaller particles compared to the other samples resulting in absorbing shorter wavelengths. So this sample is less absorbing compared to the other samples in the region of interest. Hence, we can firmly say that the photodetection in Au nanoisland photodetectors is based on hot-electrons generated through non-radiative decay of the localized surface plasmons.

Randomness of the size and distribution of Au nanoparticles leads to broadband photodetection in NIR region. We measured photoresponsivity up to 1600 nm and observed photocurrent up to 2000 nm in all of the samples. The devices in this work exhibit both wide-band and very high spectral photoresponsivity compared to that of the best reported in the literature [27,28,73,74]. Using thinner Au film and much more inexpensive methods we could fabricate photodetectors based on hot electrons with broader and higher photoresponsivity values in NIR region.

Chapter 5

Conclusions

In conclusion, we designed easy to fabricate, ultra-low-cost, and highly scalable broad-band NIR photodetectors on Silicon. These devices show broad-band photoresponsivity values without using any other enhancement method such as anti-reflection coating and back-side metallization. Our results are in the same order with those reported in literature with high-cost and slow fabrication methods [28, 74] and maximum values of narrow-band NIR photodetectors using plasmonic structures [27, 73]. The proof-of-concept demonstration of NIR photodetection via simple methods was done in this study and is promising for civilian NIR imaging which can be used in large industries like automotive, security, and telecommunication.

In future studies, one can consider other simple methods like drop-casting of synthesized nanoparticles of metals, which gives better control on the size distribution of the particles to overcome the problems which hindered us from fabricating photodetectors based on Ag or Al. Using interlayer dielectric films, we can shift the plasmon resonances further towards infrared as well as suppressing the dark current of the photodetectors. Also in this configuration which is based on quantum tunneling, more CMOS compatible nanoparticles which show plasmonic effect in infrared such as Silicon can be used instead of metals.

Bibliography

[1] M. Herrscher, M. Grundmann, E. Droge, S. Kollakowski, E. Bottcher, and D. Bimberg, "Epitaxial liftoff ingaas/inp msm photodetectors on si," *Electron. Lett.*, vol. 31, no. 16, pp. 1383–1384, 1995.

[2] R. H. Walden, "A review of recent progress in inp-based optoelectronic integrated circuit receiver front-ends," *Int. J. High Speed Electron. Syst.*, vol. 9, no. 02, pp. 631–642, 1998.

[3] J. Brouckaert, G. Roelkens, D. Van Thourhout, and R. Baets, "Thin-film iii–v photodetectors integrated on silicon-on-insulator photonic ics," *J. Lightwave Technol.*, vol. 25, no. 4, pp. 1053–1060, 2007.

[4] L. G. Burriesci, "Nircam instrument overview," in *Optics & Photonics 2005*, pp. 590403–590403, International Society for Optics and Photonics, 2005.

[5] *Overview of SWIR detectors, cameras, and applications*, 2008.

[6] J. B. Soole and H. Schumacher, "Ingaas metal-semiconductor-metal photodetectors for long wavelength optical communications," *IEEE J. Quantum Electron.*, vol. 27, no. 3, pp. 737–752, 1991.

[7] J. C. Campbell, "Recent advances in telecommunications avalanche photodiodes," *J. Lightwave Technol.*, vol. 25, no. 1, pp. 109–121, 2007.

[8] L. Chaerle and D. Van Der Straeten, "Seeing is believing: imaging techniques to monitor plant health," *Biochimica et Biophysica Acta (BBA)-Gene Structure and Expression*, vol. 1519, no. 3, pp. 153–166, 2001.

[9] B. G. Osborne, T. Fearn, and P. H. Hindle, *Practical NIR spectroscopy with applications in food and beverage analysis.* Longman scientific and technical, 1993.

[10] M. Blanco and I. Villarroya, "Nir spectroscopy: a rapid-response analytical tool," *TrAC, Trends Anal. Chem.*, vol. 21, no. 4, pp. 240–250, 2002.

[11] "The center for satellite applications and research." `http://www.star.nesdis.noaa.gov/star/index.php`.

[12] A. K. Okyay, A. M. Nayfeh, K. C. Saraswat, T. Yonehara, A. Marshall, and P. C. McIntyre, "High-efficiency metal-semiconductor-metal photodetectors on heteroepitaxially grown ge on si," *Optics letters*, vol. 31, no. 17, pp. 2565–2567, 2006.

[13] A. K. Okyay, A. J. Pethe, D. Kuzum, S. Latif, D. A. Miller, and K. C. Saraswat, "Sige optoelectronic metal-oxide semiconductor field-effect transistor," *Optics letters*, vol. 32, no. 14, pp. 2022–2024, 2007.

[14] L. Tang, S. E. Kocabas, S. Latif, A. K. Okyay, D.-S. Ly-Gagnon, K. C. Saraswat, and D. A. Miller, "Nanometre-scale germanium photodetector enhanced by a near-infrared dipole antenna," *Nature Photonics*, vol. 2, no. 4, pp. 226–229, 2008.

[15] H.-Y. Yu, S. Ren, W. S. Jung, A. K. Okyay, D. A. Miller, and K. C. Saraswat, "High-efficiency pin photodetectors on selective-area-grown ge for monolithic integration," *Electron Device Letters, IEEE*, vol. 30, no. 11, pp. 1161–1163, 2009.

[16] O. Fidaner, A. K. Okyay, J. E. Roth, R. K. Schaevitz, Y.-H. Kuo, K. C. Saraswat, J. S. Harris, and D. A. Miller, "Ge–sige quantum-well waveguide photodetectors on silicon for the near-infrared," *Photonics Technology Letters, IEEE*, vol. 19, no. 20, pp. 1631–1633, 2007.

[17] H.-Y. Yu, J.-H. Park, A. K. Okyay, and K. C. Saraswat, "Selective-area high-quality germanium growth for monolithic integrated optoelectronics," *Electron Device Letters, IEEE*, vol. 33, no. 4, pp. 579–581, 2012.

[18] E. Onaran, M. C. Onbasli, A. Yesilyurt, H. Y. Yu, A. M. Nayfeh, and A. K. Okyay, "Silicon-germanium multi-quantum well photodetectors in the near infrared," *Optics express*, vol. 20, no. 7, pp. 7608–7615, 2012.

[19] Y. Kang, H.-D. Liu, M. Morse, M. J. Paniccia, M. Zadka, S. Litski, G. Sarid, A. Pauchard, Y.-H. Kuo, H.-W. Chen, *et al.*, "Monolithic germanium/silicon avalanche photodiodes with 340 ghz gain–bandwidth product," *Nature Photonics*, vol. 3, no. 1, pp. 59–63, 2008.

[20] "Intel milestone confirms light beams can replace electronic signals for future computers." `http://www.intel.com/pressroom/archive/releases/2010/20100727comp_sm.htm`.

[21] "Mxc* optical connector technology is becoming available." `http://www.intel.com/content/www/us/en/research/intel-labs-silicon-photonics-mxc-connector.html`.

[22] F. Shepherd Jr, A. Yang, and R. Taylor, "A 1 to 2 μm silicon avalanche photodiode," *Proc. IEEE*, vol. 58, no. 7, pp. 1160–1162, 1970.

[23] M. Casalino, L. Sirleto, M. Iodice, N. Saffioti, M. Gioffrè, I. Rendina, and G. Coppola, "Cu/p-si schottky barrier-based near infrared photodetector integrated with a silicon-on-insulator waveguide," *Applied Physics Letters*, vol. 96, no. 24, p. 241112, 2010.

[24] M. Casalino, L. Sirleto, L. Moretti, and I. Rendina, "A silicon compatible resonant cavity enhanced photodetector working at 1.55 μm," *Semiconductor Science and Technology*, vol. 23, no. 7, p. 075001, 2008.

[25] A. Akbari and P. Berini, "Schottky contact surface-plasmon detector integrated with an asymmetric metal stripe waveguide," *Appl. Phys. Lett.*, vol. 95, no. 2, p. 021104, 2009.

[26] A. Akbari, R. N. Tait, and P. Berini, "Surface plasmon waveguide schottky detector," *Opt. Express*, vol. 18, no. 8, pp. 8505–8514, 2010.

[27] A. Sobhani, M. W. Knight, Y. Wang, B. Zheng, N. S. King, L. V. Brown, Z. Fang, P. Nordlander, and N. J. Halas, "Narrowband photodetection in the

near-infrared with a plasmon-induced hot electron device," *Nat. Commun.*, vol. 4, p. 1643, 2013.

[28] M. W. Knight, H. Sobhani, P. Nordlander, and N. J. Halas, "Photodetection with active optical antennas," *Science*, vol. 332, no. 6030, pp. 702–704, 2011.

[29] S. M. Sze and K. K. Ng, *Physics of semiconductor devices.* John Wiley & Sons, 2006.

[30] C. Kittel and P. McEuen, *Introduction to solid state physics*, vol. 8. Wiley New York, 1976.

[31] D. Miller, "Semiconductor optoelectronic devices," 2000.

[32] W. Chow, "Theory of phonon-assisted optical absorption in semiconductors. i.," *Phys. Rev.*, vol. 185, pp. 1056–1061, Sep 1969.

[33] E. Abers, *Quantum mechanics.* Upper Saddle River, N.J: Pearson Education, 2004.

[34] N. V. Tkachenko, *Optical spectroscopy: methods and instrumentations.* Elsevier, 2006.

[35] M. Casalino, G. Coppola, M. Iodice, I. Rendina, and L. Sirleto, "Near-infrared sub-bandgap all-silicon photodetectors: state of the art and perspectives," *Sensors*, vol. 10, no. 12, pp. 10571–10600, 2010.

[36] A. Einstein, "Über einen die erzeugung und verwandlung des lichtes betreffenden heuristischen gesichtspunkt," *Annalen der Physik*, vol. 322, no. 6, pp. 132–148, 1905.

[37] R. H. Fowler, "The analysis of photoelectric sensitivity curves for clean metals at various temperatures," *Phys. Rev.*, vol. 38, no. 1, p. 45, 1931.

[38] V. L. Dalal, "Simple model for internal photoemission," *Journal of Applied Physics*, vol. 42, no. 6, pp. 2274–2279, 1971.

[39] A. J. Leenheer, P. Narang, N. S. Lewis, and H. A. Atwater, "Solar energy conversion via hot electron internal photoemission in metallic nanostructures: Efficiency estimates," *Journal of Applied Physics*, vol. 115, no. 13, 2014.

[40] J. Tersoff, "Schottky barrier heights and the continuum of gap states," *Physical Review Letters*, vol. 52, no. 6, p. 465, 1984.

[41] J. Bardeen, "Surface states and rectification at a metal semi-conductor contact," *Physical Review*, vol. 71, no. 10, p. 717, 1947.

[42] S. E. Swirhun, *Characterization of majority and minority carrier transport in heavily doped silicon.* PhD thesis, 1987.

[43] M. A. Nazirzadeh, F. B. Atar, B. B. Turgut, and A. K. Okyay, "Random sized plasmonic nanoantennas on silicon for low-cost broad-band near-infrared photodetection," *Scientific reports*, vol. 4, 2014.

[44] F. B. Atar, E. Battal, L. E. Aygun, B. Daglar, M. Bayindir, and A. K. Okyay, "Plasmonically enhanced hot electron based photovoltaic device," *Opt. Express*, vol. 21, no. 6, pp. 7196–7201, 2013.

[45] F. Wang and N. A. Melosh, "Plasmonic energy collection through hot carrier extraction," *Nano Lett.*, vol. 11, no. 12, pp. 5426–5430, 2011.

[46] M. W. Knight, L. Liu, Y. Wang, L. Brown, S. Mukherjee, N. S. King, H. O. Everitt, P. Nordlander, and N. J. Halas, "Aluminum plasmonic nanoantennas," *Nano letters*, vol. 12, no. 11, pp. 6000–6004, 2012.

[47] M. W. Knight, N. S. King, L. Liu, H. O. Everitt, P. Nordlander, and N. J. Halas, "Aluminum for plasmonics," *ACS nano*, vol. 8, no. 1, pp. 834–840, 2013.

[48] S. A. Maier, *Plasmonics: Fundamentals and Applications: Fundamentals and Applications.* Springer, 2007.

[49] P. Drude, "Zur elektronentheorie der metalle," *Annalen der Physik*, vol. 306, no. 3, pp. 566–613, 1900.

[50] A. Vial, A.-S. Grimault, D. Macías, D. Barchiesi, and M. L. de La Chapelle, "Improved analytical fit of gold dispersion: Application to the modeling of extinction spectra with a finite-difference time-domain method," *Physical Review B*, vol. 71, no. 8, p. 085416, 2005.

[51] E. Devaux, T. W. Ebbesen, J.-C. Weeber, and A. Dereux, "Launching and decoupling surface plasmons via micro-gratings," *Applied physics letters*, vol. 83, no. 24, pp. 4936–4938, 2003.

[52] E. Kretschmann and H. Raether, "Radiative decay of non radiative surface plasmons excited by light(surface plasma waves excitation by light and decay into photons applied to nonradiative modes)," *Zeitschrift Fuer Naturforschung, Teil A*, vol. 23, p. 2135, 1968.

[53] A. Otto, "Excitation of nonradiative surface plasma waves in silver by the method of frustrated total reflection," *Zeitschrift für Physik*, vol. 216, no. 4, pp. 398–410, 1968.

[54] W. Knoll, "Interfaces and thin films as seen by bound electromagnetic waves," *Annual Review of Physical Chemistry*, vol. 49, no. 1, pp. 569–638, 1998.

[55] D. B. Pedersen and E. Duncan, "Surface plasmon resonance spectroscopy of gold nanoparticle-coated substrates: Use as an indicator of exposure to chemical warfare simulants," tech. rep., DTIC Document, 2005.

[56] C. Fragstein and U. Kreibig, "Studies of intersystem crossing dynamics in acetylene," *Phys*, vol. 224, p. 306, 1969.

[57] S. Eustis and M. A. El-Sayed, "Why gold nanoparticles are more precious than pretty gold: noble metal surface plasmon resonance and its enhancement of the radiative and nonradiative properties of nanocrystals of different shapes," *Chemical Society Reviews*, vol. 35, no. 3, pp. 209–217, 2006.

[58] M. M. Alvarez, J. T. Khoury, T. G. Schaaff, M. N. Shafigullin, I. Vezmar, and R. L. Whetten, "Optical absorption spectra of nanocrystal gold molecules," *The Journal of Physical Chemistry B*, vol. 101, no. 19, pp. 3706–3712, 1997.

[59] U. Kreibig and M. Vollmer, "Optical properties of metal clusters," 1995.

[60] M. Meier and A. Wokaun, "Enhanced fields on large metal particles: dynamic depolarization," *Optics Letters*, vol. 8, no. 11, pp. 581–583, 1983.

[61] H. Kuwata, H. Tamaru, K. Esumi, and K. Miyano, "Resonant light scattering from metal nanoparticles: Practical analysis beyond rayleigh approximation," *Applied physics letters*, vol. 83, no. 22, pp. 4625–4627, 2003.

[62] G. Mie, "Beiträge zur optik trüber medien, speziell kolloidaler metallösungen," *Annalen der physik*, vol. 330, no. 3, pp. 377–445, 1908.

[63] T. Kokkinakis and K. Alexopoulos, "Observation of radiative decay of surface plasmons in small silver particles," *Physical Review Letters*, vol. 28, no. 25, p. 1632, 1972.

[64] J. Endriz and W. Spicer, "Surface-plasmon-one-electron decay and its observation in photoemission," *Phys. Rev. Lett.*, vol. 24, no. 2, p. 64, 1970.

[65] A. Wokaun, J. Gordon, and P. Liao, "Radiation damping in surface-enhanced raman scattering," *Physical Review Letters*, vol. 48, no. 14, p. 957, 1982.

[66] S. Link and M. A. El-Sayed, "Shape and size dependence of radiative, non-radiative and photothermal properties of gold nanocrystals," *International Reviews in Physical Chemistry*, vol. 19, no. 3, pp. 409–453, 2000.

[67] K.-C. Lee, S.-J. Lin, C.-H. Lin, C.-S. Tsai, and Y.-J. Lu, "Size effect of ag nanoparticles on surface plasmon resonance," *Surf. Coat. Technol.*, vol. 202, no. 22, pp. 5339–5342, 2008.

[68] R. A. Ismail, A. Al-Naimi, and A. A. Al-Ani, "Studies on fabrication and characterization of a high-performance al-doped zno/n-si (1 1 1) heterojunction photodetector," *Semicond. Sci. Technol.*, vol. 23, no. 7, p. 075030, 2008.

[69] S. Franzen, "Surface plasmon polaritons and screened plasma absorption in indium tin oxide compared to silver and gold," *The Journal of Physical Chemistry C*, vol. 112, no. 15, pp. 6027–6032, 2008.

[70] E. D. Palik, *Handbook of optical constants of solids*, vol. 3. Academic press, 1998.

[71] P. B. Johnson and R.-W. Christy, "Optical constants of the noble metals," *Phys. Rev. B*, vol. 6, no. 12, p. 4370, 1972.

[72] M. Rycenga, C. M. Cobley, J. Zeng, W. Li, C. H. Moran, Q. Zhang, D. Qin, and Y. Xia, "Controlling the synthesis and assembly of silver nanostructures for plasmonic applications," *Chemical reviews*, vol. 111, no. 6, pp. 3669–3712, 2011.

[73] W. Li and J. G. Valentine, "Metamaterial perfect absorber based hot electron photodetection," *Nano Lett.*, 2014.

[74] K.-T. Lin, H.-L. Chen, Y.-S. Lai, and C.-C. Yu, "Silicon-based broadband antenna for high responsivity and polarization-insensitive photodetection at telecommunication wavelengths," *Nat. Commun.*, vol. 5, 2014.

Appendix A

AZO Deposition Recipe

More detailed AZO deposition recipe using ALD is provided in Table A.1.

Instruction	#	Value	Unit	Description
Heater	8	250	°C	Heater setpoint
Heater	9	250	°C	Heater setpoint
Stabilize	8			Waiting for stabilization
Stabilize	9			Waiting for stabilization
flow		20	sccm	N_2 flow setpoint
wait		300	s	
pulse	0	0.1	ms	H_2O purge duration
wait		5	s	
pulse	2	0.01	ms	DEZ purge duration
wait		5	s	
goto	6	28		ZnO deposition cycle number
pulse	0	0.1	ms	H_2O purge duration
wait		5	s	
pulse	3	0.03	ms	TMA purge duration
wait		5	s	
goto	6	16		Al_2O_3 deposition cycle number
pulse	0	0.1	ms	H_2O purge duration

wait		5	s	
pulse	2	0.01	ms	DEZ purge duration
wait		5	s	
goto	16	28		Total AZO deposition cycle number
wait		5	s	
flow		5	sccm	N_2 flow setpoint
heater	8	80	°C	Heater setpoint
heater	9	80	°C	Heater setpoint
line ac out	2			
line ac out	1			
stopvalve		1		

Table A.1: AZO deposition recipe using ALD. Diethylzinc (DEZ) and Trimethylaluminium (TMA) precursors was used for ZnO and Al_2O_3 layer deposition steps, respectively.

Appendix B

Experimental Optical Properties of AZO

The experimental refractive index (n) and extinction coefficient (k) of the AZO film is provided in Table. B.1.

Wavelength (nm)	n	k
600	2.02921111	7.87252641e-014
610	2.01883421	6.30041861e-014
620	2.00895536	5.07861724e-014
630	1.99954318	4.12186485e-014
640	1.99056875	3.36724627e-014
650	1.98200533	2.7679493e-014
660	1.97382819	2.28886763e-014
670	1.96601446	1.90347435e-014
680	1.95854291	1.59158005e-014
690	1.95139385	1.3377121e-014
700	1.94454898	1.12993378e-014
710	1.93799129	9.58977437e-015
720	1.93170494	8.17603615e-015
730	1.92567515	7.00123901e-015

740	1.91988817	6.02043344e-015
750	1.91433111	5.1979074e-015
760	1.90899197	4.50513951e-015
770	1.90385949	3.91923644e-015
780	1.89892314	3.42173317e-015
790	1.89417307	2.99766679e-015
800	1.8896	2.63485755e-015
810	1.88519526	2.32334813e-015
820	1.88095068	2.05496387e-015
830	1.8768586	1.82296644e-015
840	1.87291179	1.62177969e-015
850	1.86910346	1.44677177e-015
860	1.8654272	1.2940811e-015
870	1.86187699	1.16047687e-015
880	1.85844711	1.04324678e-015
890	1.85513219	9.40106234e-016
900	1.85192716	8.49124711e-016
910	1.84882721	7.6866583e-016
920	1.84582779	6.97338332e-016
930	1.8429246	6.33955904e-016
940	1.84011358	5.77504117e-016
950	1.83739086	5.27113128e-016
960	1.83475278	4.82035084e-016
970	1.83219587	4.4162534e-016
980	1.82971683	4.05326812e-016
990	1.82731253	3.72656912e-016
1000	1.82498	3.43196579e-016
1010	1.82271641	3.16581085e-016
1020	1.82051907	2.92492266e-016
1030	1.81838542	2.70651975e-016
1040	1.81631302	2.50816528e-016

1050	1.81429955	2.32771992e-016
1060	1.81234279	2.16330172e-016
1070	1.81044064	2.01325189e-016
1080	1.80859108	1.87610553e-016
1090	1.8067922	1.75056657e-016
1100	1.80504215	1.63548619e-016
1110	1.80333919	1.52984431e-016
1120	1.80168163	1.43273358e-016
1130	1.80006789	1.34334557e-016
1140	1.79849643	1.26095879e-016
1150	1.79696578	1.18492829e-016
1160	1.79547455	1.11467668e-016
1170	1.7940214	1.0496862e-016
1180	1.79260503	9.89491933e-017
1190	1.79122421	9.33675735e-017
1200	1.78987778	8.81861041e-017
1210	1.78856459	8.33708234e-017
1220	1.78728355	7.88910609e-017
1230	1.78603364	7.47190812e-017
1240	1.78481384	7.08297706e-017
1250	1.7836232	6.72003597e-017
1260	1.7824608	6.38101797e-017
1270	1.78132574	6.06404449e-017
1280	1.78021719	5.76740611e-017
1290	1.77913431	5.48954553e-017
1300	1.77807633	5.22904235e-017
1310	1.77704249	4.98459963e-017
1320	1.77603205	4.75503187e-017
1330	1.77504432	4.53925421e-017
1340	1.77407861	4.33627291e-017
1350	1.77313429	4.1451767e-017

1430	1.76627879	2.95671727e-017
1440	1.76550123	2.84193732e-017
1450	1.76473971	2.73310533e-017
1460	1.76399379	2.62984738e-017
1470	1.76326303	2.53181684e-017
1480	1.76254704	2.43869211e-017
1490	1.76184542	2.35017457e-017
1500	1.76115778	2.26598673e-017
1510	1.76048376	2.18587056e-017
1520	1.75982299	2.10958591e-017
1530	1.75917514	2.03690912e-017
1540	1.75853987	1.96763177e-017
1550	1.75791686	1.90155944e-017
1560	1.75730579	1.83851071e-017
1570	1.75670635	1.77831612e-017
1580	1.75611827	1.72081733e-017
1590	1.75554124	1.66586624e-017
1600	1.754975	1.61332426e-017
1610	1.75441928	1.56306163e-017
1620	1.75387381	1.51495676e-017
1630	1.75333836	1.46889567e-017
1640	1.75281267	1.4247714e-017
1650	1.75229651	1.38248358e-017
1660	1.75178965	1.34193793e-017
1670	1.75129187	1.30304585e-017
1680	1.75080295	1.26572402e-017
1690	1.75032268	1.22989406e-017
1700	1.74985087	1.19548218e-017
1710	1.7493873	1.16241888e-017
1720	1.7489318	1.13063868e-017
1730	1.74848418	1.10007983e-017

1740	1.74804425	1.07068406e-017
1750	1.74761184	1.04239641e-017
1760	1.74718678	1.01516496e-017
1770	1.7467689	9.88940662e-018
1780	1.74635805	9.63677146e-018
1790	1.74595406	9.39330571e-018
1800	1.74555679	9.15859455e-018
1810	1.74516608	8.93224531e-018
1820	1.7447818	8.71388615e-018
1830	1.7444038	8.50316474e-018
1840	1.74403195	8.29974717e-018
1850	1.74366611	8.10331676e-018
1860	1.74330615	7.91357311e-018
1870	1.74295195	7.7302311e-018
1880	1.7426034	7.55302002e-018
1890	1.74226035	7.38168271e-018
1900	1.74192271	7.21597483e-018
1910	1.74159036	7.05566408e-018
1920	1.74126319	6.90052952e-018
1930	1.7409411	6.75036097e-018
1940	1.74062397	6.60495839e-018
1950	1.7403117	6.46413128e-018
1960	1.74000421	6.32769824e-018
1970	1.73970138	6.19548639e-018
1980	1.73940313	6.06733094e-018
1990	1.73910937	5.94307476e-018
2000	1.73882	5.82256799e-018

Table B.1: Extracted n-k data of AZO film using ellipsometry.

Appendix C

Alternative Fabrication Methods

C.1   E-beam Lithography

E-beam lithography is a high resolution lithography technique which can resolve sub-100 nm features. In first step of the study, we used e-beam lithography technique to fabricate sample devices to make calibrate our fabrication and characterization setup. Fig C.1 shows two magnifications of the fabricated devices using e-beam lithography.
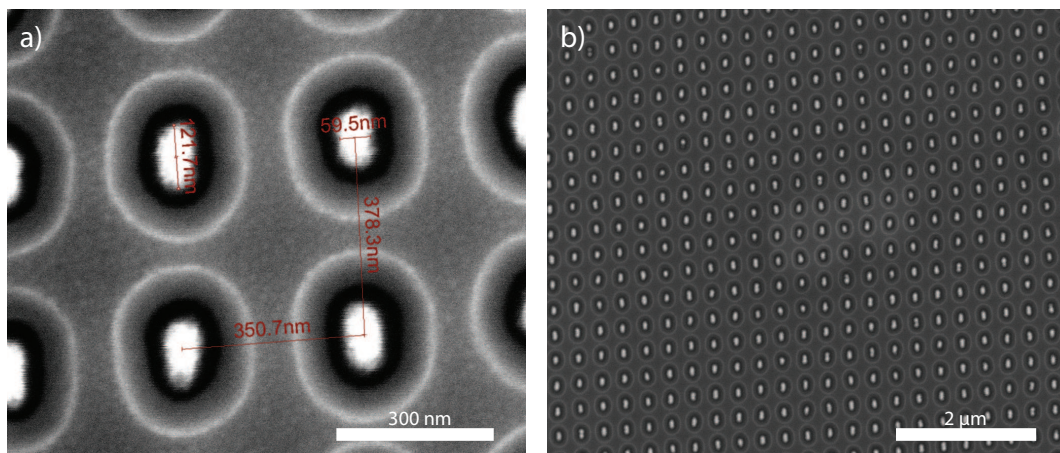

Figure C.1: SEM images of samples patterned using e-beam lithography.

This technique is well studied in the literature [28]. So we used this technique for both calibration of our characterization setup and verifying the promising results of the simulations. Since e-beam lithography is a slow and costly process, we didn't used this method for the rest of our study.
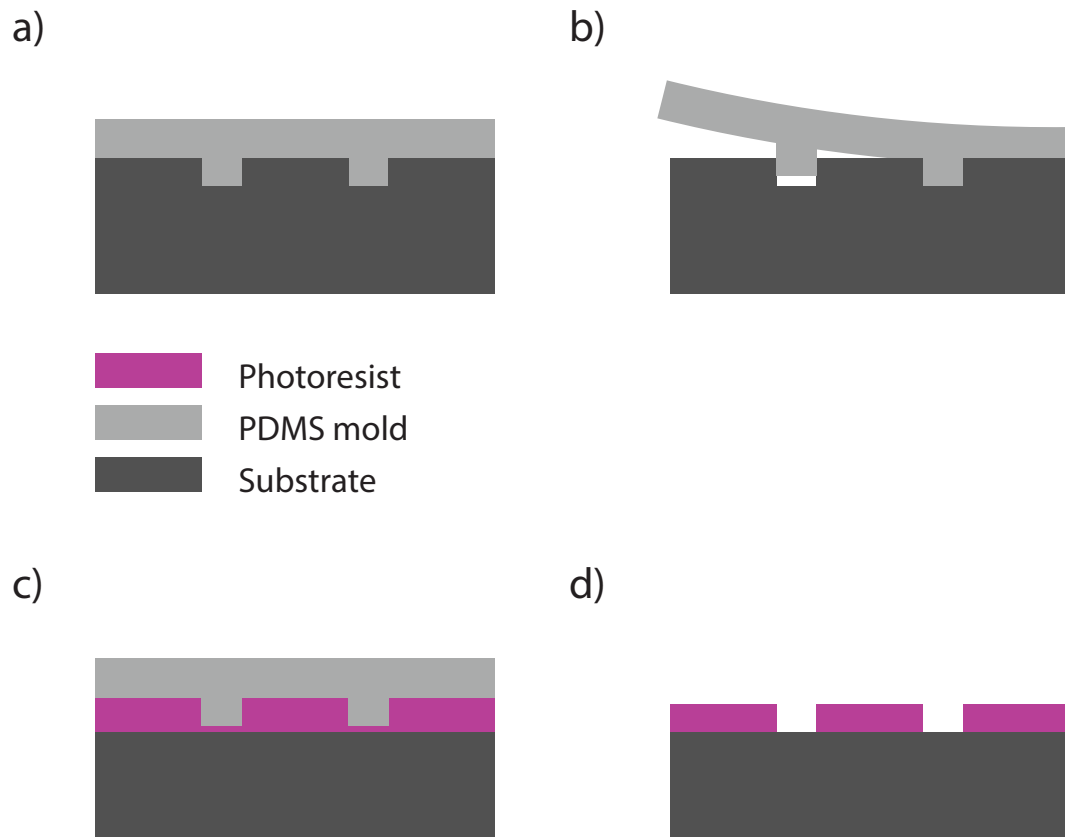
C.2 Nanoimprint Lithography

Figure C.2: Illustration of nanoimprint lithography method. (a) Deposition of PDMS on the sample. PDMS takes the shape of the sample. (b) Peeling off the PDMS mold. (c) Imprinting the pattern under pressure and heat. (d) Peeling off the PDMS mold and dry etching the sample to achieve the desired pattern.

Nanoimprint lithography is a low-cost, fast lithography, and high resolution method. First the desired pattern is generated using a high resolution technique. Then the patterns are transferred to a mold which is usually Polydimethylsiloxane (PDMS). PDMS is a mixture of Silicone elastomer (base) and its corresponding
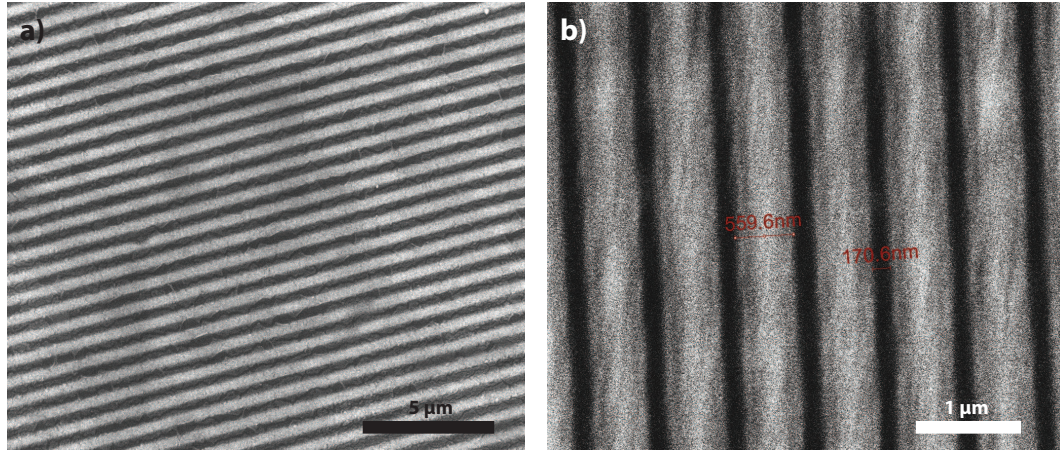
Figure C.3: SEM images of samples patterned using nanoimprint lithography.

curing agent. Carefully mixing a (10:1) base to curing agent mixture ratio for about 10 minutes guarantees a uniform distribution. Then for removing the air bubbles from that, we put the mixture in the desiccator for about an hour (until all the air bubbles are removed). Then we put the sample with the original patterns to a container and carefully pour the PDMS on it, leaving the container on a hot plate at 150°C. The PDMS will dry and be ready for peeling off. Then slowly we can peel the PDMS mold (a mold can be used for lots of times without getting damaged) (Fig. C.2a). Then we gently peel it from the sample (Fig. C.2b). Now we can re-transfer the pattern from the PDMS mold to a die coated with photoresist under high and conformal pressure (Fig. C.2c). Also the die should be heated to temperatures slightly higher than the glass transient temperature of the photoresist. This allows the transfer of the pattern to the photoresist film and also hardens it after cool down. Then a short dry etching process should be run to completely remove the photoresist from unwanted places (Fig. C.2d).

Since this method needs high resolution lithography techniques as starting point, we tried using the patterns of commercial DVDs as starting point for our nanoimprint lithography and fabricated some samples (Fig. C.3).